Control and Interfacing of Three Phase Grid Connected Photovoltaic Systems

by

Ahmed Said Khalifa

A thesis
presented to the University of Waterloo
in fulfillment of the
thesis requirement for the degree of
Master of Applied Science
in
Electrical and Computer Engineering

Waterloo, Ontario, Canada, 2010

AUTHOR'S DECLARATION

I hereby declare that I am the sole author of this thesis. This is a true copy of the thesis, including any required final revisions, as accepted by my examiners.

I understand that my thesis may be made electronically available to the public.

Abstract

Solar power is considered a very promising source for electric power generation. The abundance of sunlight over a large area of the earth surface gives rise to several applications of photovoltaic systems. Electricity can be generated from sunlight either directly by employing the photovoltaic effect, or by using energy from the sun to heat up a working fluid that can be used to power up electricity generators. These two technologies are widely used today to provide power to either stand-alone loads or for connection to the power system grid.

Maximum power point tracking (MPPT) is a very important consideration that is taken into account when building a new photovoltaic power system. This is needed in order to extract maximum power output from a PV array under varying atmospheric conditions to maximize the return on initial investments.

Several techniques have been used to tackle this problem including perturb and observe (P&O), incremental conductance (IncCond) and fuzzy logic based algorithms. Judging between these techniques is based on their speed of locating the maximum power point (MPP) of a PV array under given atmospheric conditions, besides the cost and complexity of implementing them. The P&O and IncCond algorithms have a low implementation complexity but their tracking speed is slow. Fuzzy logic techniques are faster but suffer from high implementation complexity.

One of the goals of this thesis is to present an MPPT algorithm implementation that is based on the fractional open circuit voltage method. This technique is easy to implement and offers a fast tracking speed for the MPP of a PV array. It provides an approximation within 4-5% of the maximum power point, which is a tradeoff between the speed and accuracy of operation around the MPP. It offers a speed advantage in grid connected PV systems. The P&O algorithm, which is very common, is difficult to implement under these conditions due to its poor response time.

There is also a need for developing control techniques for three phase grid connected PV systems including a method for DC link voltage control that can stabilize the voltage at the inverter input. This area of research is currently growing with the increase in number of PV installations backed up by government incentives in several countries. In addition to the previously mentioned points, this work is intended to be used in further research to replace the representation of PV arrays as a simple DC source when included in power system studies. That is a basic assumption and does not take into consideration the various dynamics caused by changing solar irradiation and surface temperature of the array.

Acknowledgements

First and foremost, I thank God for helping me complete this work and reach this stage of life. Words are not enough to express my gratitude for all his blessings.

I would like to thank my supervisor, Dr. Ehab El Saadany, for his support and guidance over the course of my research and for the many discussions we had that helped bring out this work. I would also like to thank Dr. Mehrdad Kazerani and Dr. Tarek AbdelGalil for taking the time to read my thesis.

My deepest gratitude goes to my family members, especially my mother and father for their patience and support. I thank all my brothers and sisters as well.

Thanks to my friends Ahmed Bayoumy, Ahmed Shehata, Karim El Rayes, Ahmed El Hadidy, Farouk Mokaddem and Nizar Mrabet for making Waterloo feel like home.

Dedication

In memory of my grandparents

Table of Contents

List of Figures

List of Tables

Chapter 1
Introduction

The Aim of this chapter is to provide the research motivations related to grid interconnection of Photovoltaic arrays and the objectives to be reached from it. An outline is presented as well to give a summary of the topics covered in each chapter.

1.1 Research Motivation

As the world electricity consumption rapidly increases with population growth, new power generation capacities are required to cover that demand. In a recent study by the U.S Energy Information Administration (EIA), the total electricity generation of the world is expected to increase from 18.8 trillion kWh in 2007 to 25.2 trillion kWh in 2020 and 35.2 trillion kWh in 2035 [1] for a total increase of 87 % over the forecast period. The expected energy consumption trend is shown in figure 1-1.

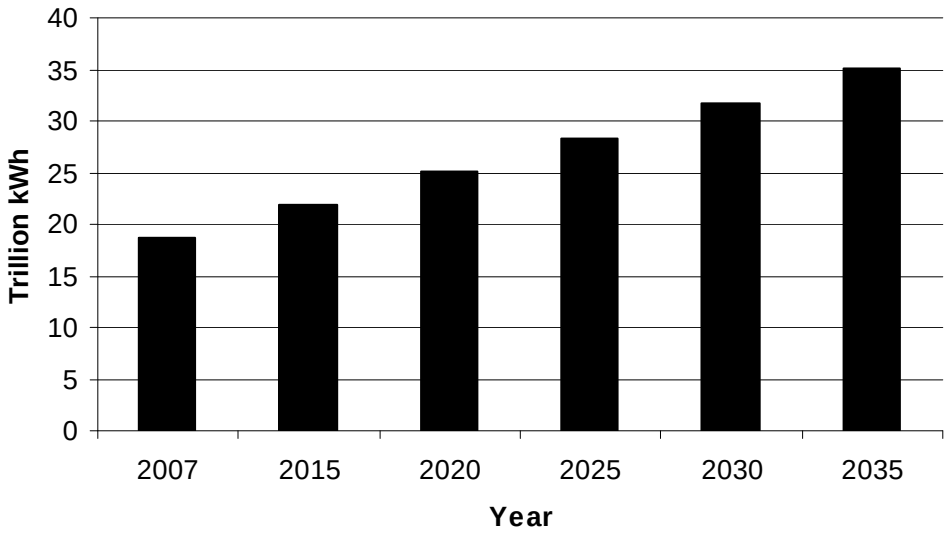

Figure 1-1: Total expected electricity generation in the world from 2007 to 2030 [1].

Power generation stations rely on multiple fuel sources to cover power demand. Coal is the most used fuel type because of its abundance and low cost. A drawback of fossil fuels is the large amount of carbon dioxide gas emissions that cause the greenhouse effect. The world electricity generation expectations by fuel type are illustrated in figure 1-2. Given the volatility and high price of liquid fuels including oil, they do not experience significant growth in terms of electricity generation. Coal based power generation expectations are susceptible to variations as many countries introduce carbon emission regulations, which may lead to reductions in the number of coal-based power stations. Renewable energy sources, on the contrary, are the fastest growing source of electricity generation with a growth rate of 3% each year mainly driven by expansion in hydro and wind powers [1]. The rest of renewable energy sources including geothermal and solar powers are still not economically competitive with fossil fuel generation.

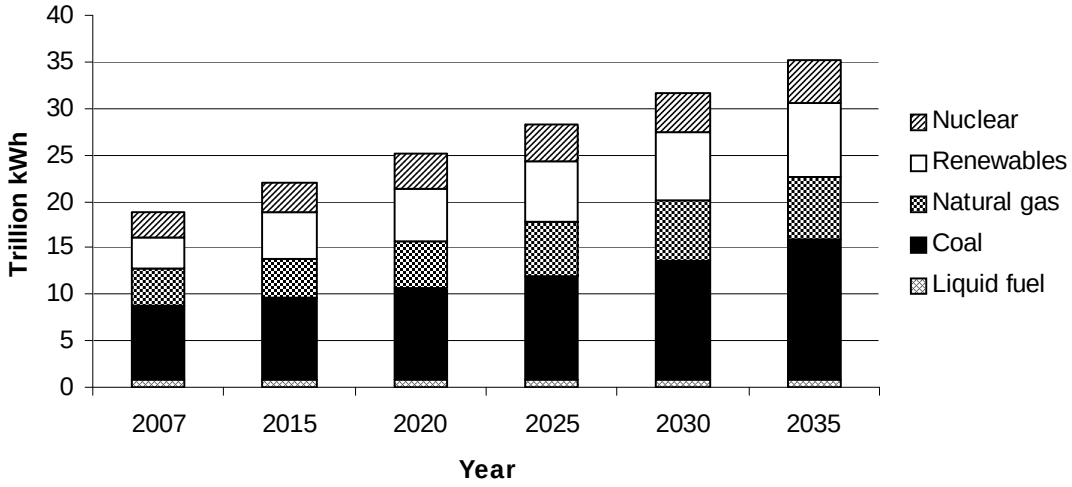

Figure 1-2: World expected electricity production by fuel source from 2007 to 2035 [1].

The renewable energy expected generation in year 2035 is broken down as shown in figure 1-3. It is clear that both hydro and wind powers dominate the share of renewable sources at 85% of the

expected renewable energy contribution, while solar and geothermal energies are expected to contribute about 2% each. The cost per kWh of generated energy for solar power is high compared to fossil fuel based sources, which is why it does not contribute with a significant share.

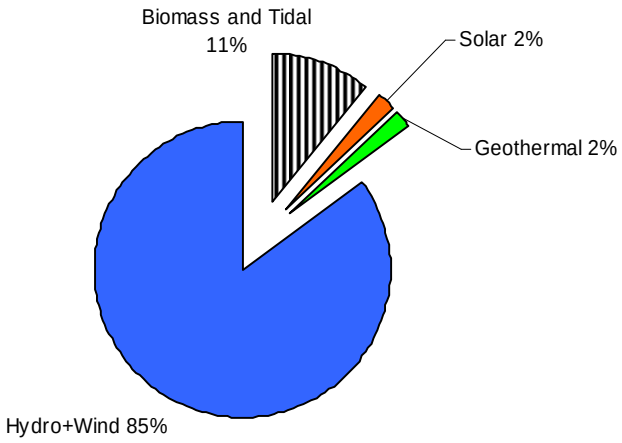

Figure 1-3: Breakdown of renewable energy sources in year 2035

To ease the impact of the cost problem in installing new renewable energy capacities, some governments provide incentives to help reduce cost of installing new systems. Of main interest to this research is the expansion of grid connected photovoltaic arrays. According to the International Energy Agency (IEA), about 5.56 GW of new PV capacity was installed in year 2008. This brought the total installed PV power in IEA participating countries to 13.4 GW [2]. Around 96% of that capacity was installed in Germany, Spain, Italy, the United States of America, Korea and Japan. Grid connected photovoltaic compose the majority of that installed capacity. The government of Ontario, Canada, has introduced the feed-in-tariff (FIT) program in 2009 with the aim of phasing out coal based electricity generation stations. Ontario Power Authority (OPA) is the entity in charge of

implementing the FIT program, which it claims to be North America's first guaranteed pricing structure for renewable energy power generation. Under this program, owners of grid-connected PV systems are contracted to sell their generated power back to the power system grid. According to OPA, the pricing structure is set at 80 ¢/kWh for PV systems with capacities below 10 kW_p for a contract period of 20 years [3]. Large ground mounted PV systems, on the other hand, have a price of 44.3 ¢/kWh for the same contract period. The OPA pricing scheme for some grid connected renewable energy systems is listed in table 1-1.

Table 1-1: FIT program pricing structure, Ontario Power Authority [3]

Energy source	Size	Contract price ¢/kWh	Percentage escalated
Solar PV			
Rooftop	≤ 10 kW	80.2	0%
Rooftop	10 - 250 kW	71.3	0%
Rooftop	250 - 500 kW	63.5	0%
Rooftop	above 500 kW	53.9	0%
Ground mounted	≤ 10 kW	64.2	0%
Ground mounted	10 kW- 10 MW	44.3	0%
Biogas			
On-farm	≤ 100 kW	19.5	20%
On-farm	100 - 250 kW	18.5	20%
Biogas	less than 500 kW	16	20%
Biogas	500 kW- 10 MW	14.7	20%
Biogas	above 10 MW	10.4	20%
Wind			
Onshore	Any size	13.5	20%
Offshore	Any size	19	20%

The output of solar PV arrays is dependent on the level of solar irradiance and surface temperature of the array itself. Maximum power output from the array can be achieved by a combination of mechanical solar trackers to maximize the amount of light received, and a maximum power point

tracking (MPPT) algorithm to operate the PV array around its maximum power output for a given load under varying atmospheric conditions. The task of MPPT for a fixed load is similar to impedance matching, where a power electronic DC/DC converter tries to match the load impedance to the ratio between voltage and current of the array at the maximum power point (MPP). One of the most common algorithms to achieve this task is the Perturb and Observe (P&O) algorithm. It perturbs the duty cycle of the DC/DC converter switch and then observes the resulting change on the delivered power to the load. The algorithm performs this systematically until any resulting change in the duty cycle causes the power delivered to the load to decrease.

The situation in grid connected systems is different, however, since the load impedance is not fixed. In addition, a fast MPPT algorithm is needed to reach maximum output power from the array under quick variations like load or weather changes. Although the incremental conductance technique is faster than P&O, it is still relatively slow for grid connected applications as it performs computations that help it keep the sense of direction towards the maximum power point. As for fuzzy logic based techniques, they suffer from implementation complexity and require previous experience to carefully set the fuzzification parameters for the algorithm despite their quick response after careful tuning.

The aim here is to estimate the PV array voltage at the maximum power point using test cells that keep track of the current radiation and temperature levels, and then use this information to drive the main PV array to maximum power output. This technique is simple and offers fast dynamic response to variations in atmospheric conditions. But the tradeoff is that it does so by approximating the MPP of the array.

The control approach in designing the grid connected PV system employs two control loops: an outer control loop that is used to regulate the output power from the PV array to the grid, and an inner

control loop that is used to regulate the injected current to the grid and keep it in phase with voltage to achieve unity power factor operation. The system was simulated using SIMULINK and a fault study was conducted to examine the behavior of the system and fault currents when the PV array was connected.

This thesis is also intended to help researchers working in the general area of distributed generation to incorporate PV arrays into their systems without having to use simplifications as a DC power source, which ignores the array dynamics, or having to implement a complex MPPT algorithm that can delay simulations significantly.

1.2 Research objectives

The goal of research done in this thesis is to develop a control strategy for three phase grid connected photovoltaic arrays. This can be summarized in the following points:

1. Use the equivalent circuit model of a PV cell to build and simulate a grid connected PV system using the open loop MPPT technique described earlier. The response to a simulated weather change depicted by a drop in solar irradiation will be investigated. The dynamic response of the algorithm is characterized by the speed it drives the PV system into maximum power operation while ensuring that the injected current remains in phase with the grid voltage to achieve a unity power factor.

2. Design the control loops to regulate output power and the injected currents respectively. The outer power loop is responsible for setting the reference signal for the inner current loop. The control signals will be used to drive a three phase voltage source inverter (VSI) to regulate the power conversion process from DC to AC. Harmonics that result during the power conversion process should be prevented from propagating into the power system grid because of their negative effects on the power system equipment and power quality.

3. Investigate the interactions between the PV system and the grid, mainly during fault conditions. The interconnection transformer of the PV array can alter the path of fault currents and affect the operation of the power system protection equipment that isolate the fault.

1.3 Thesis Outline

This thesis is divided into the following chapters:

- Chapter 2 is an overview of the main building blocks of a grid connected PV system including PV arrays and their manufacturing technologies, DC converters and three phase inverters.
- Chapter 3 goes through the control development of the grid connected PV system. The control system is divided into two main parts: control of the DC converter for maximum power extraction and control of the three phase voltage source inverter for injection of AC current into the grid. Inverter modeling and control in the *dq* frame in addition to the sinusoidal pulse width modulation (SPWM) techniques are covered for their importance in the development of the control system.
- Chapter 4 presents the simulation results to study the operation of the PV system under varying weather conditions, mainly solar irradiation. Simulation results for the system under fault conditions are also included to investigate the effect of fault current from the PV array on the operation of the power system protection devices.
- Chapter 5 is a summary and conclusion of the main points obtained in this thesis.

Chapter 2
Components of Grid-Connected Photovoltaic power systems

The aim of this chapter is to present an overview of the main building blocks in a grid connected PV system. These systems can be classified in terms of their connection to the power system grid into the following [2]:

1. Off-grid residential: This class of photovoltaic systems is used to power small homes that are not connected to the power system grid. The output of the system is used for lighting and refrigeration and other basic power needs. The capacity of the system is below 10 kW in peak output power. They are used when it is more economical to install a PV system than extending the power lines to locations that are far from the utility.

2. Off-grid commercial: PV systems that are used for commercial purposes, for example water pumping or for generating power to run telecommunication towers. The great need for power in these remote locations makes installing PV systems an economically viable alternative.

3. Grid-Connected distributed: Systems installed on rooftops of homes and buildings that sell power back to the power system. Smart meters are used to keep track of the net power, which is the difference between customer generated power and consumed power. The capacity of the system varies depending on the available surface area for PV installation.

4. Grid-connected centralized: Utility scale systems that can reach tens of megawatts of power output under optimum conditions of solar irradiation. These systems are usually ground mounted and span a large area for power harvesting. The solar PV array in Sarnia, Ontario (currently expanding to 80 MW) is an example of such systems.

As centralized grid connected PV systems comprise a large portion of the installed capacity, focus in this thesis will be mainly on it to study their performance and interactions with the power system grid.

Several components are needed to construct a grid connected PV system to perform the power generation and conversion functions, as shown in figure 2-1. A PV array is used to convert the light from the sun into DC current and voltage. A DC converter is connected to the PV array to increase its terminal voltage and provide the means to implement an MPPT technique by controlling its switching duty cycle. The output power from the array is stored temporarily in large capacitors to hold power before DC/AC power conversion. A three phase inverter is then connected to perform the power conversion of the array output power into AC power suitable for injection into the grid. Pulse width modulation control is one of the techniques used to shape the magnitude and phase of the inverter output voltage. A harmonics filter is added after the inverter to reduce the harmonics in the output current which result from the power conversion process. An interfacing transformer is connected after the filter to step up the output AC voltage of the inverter to match the grid voltage level. Protection relays and circuit breakers are used to isolate the PV system when faults occur to prevent damage to the equipment if their ratings are exceeded.

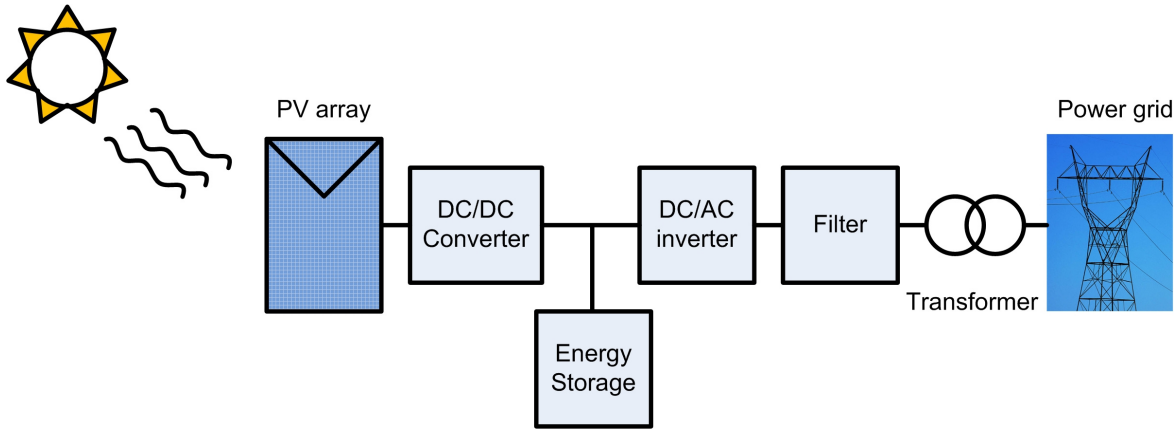

Figure 2-1: Components of a grid connected PV system.

2.1 Photovoltaic cell technologies and modeling

PV cells are classified based on the type of materials used in manufacturing them. Below are some of the common materials used to build PV cells.

2.1.1 Crystalline Silicon PV cells

Comprising 20% of the earth's crust composition, Silicon is considered the second most abundant element on earth [4]. Silicon exists in nature in the form of Silicon dioxide minerals like quartz and silicate based minerals. It has first to reach a high degree of purity before it can be used for manufacturing single crystal PV cells. High grade quartz or silicates are first treated chemically to form an intermediate silicon compound (Liquid trichlorosilane $SiHCl_3$), which is then reduced in a reaction with hydrogen to produce chunks of highly pure Silicon, about 99.9999% in purity. After that, these chunks of silicon are melted and formed into a single large crystal of Silicon through a process called the Czochralski process. The large Silicon crystal is then cut into thin wafers using special cutting equipment. These wafers are then polished and doped with impurities to form the required p-n junction of the PV cell. Antireflective coating materials are added on top of the cell to reduce light reflections and allow the cell to better absorb sunlight. A grid of contacts made of silver or aluminum is added to the cell to extract the electric current generated when it is exposed to light. The experimental efficiency of Single crystal silicon cells is about 25% or slightly higher under standard test conditions (1000 W/m^2 and 25 ˚C). However, commercial PV modules' efficiency is in the range of 12%-15% [2]. The process of producing PV cells using this technology is quite expensive, which led to development of new technologies that do not suffer from this drawback.

2.1.2 Multi-crystalline Silicon PV cells

In order to avoid the high cost of producing single crystal solar cells, cheaper multi-crystalline cells were developed. As the name implies, multi-crystalline Silicon solar cells do not have a single crystal

structure. They are rather derived from several smaller crystals that together from the cell. The grain boundaries between each crystal reduce the net electric current that can be generated because of electron recombination with defective atomic bonds. However, the cost of manufacturing cells using this technology is less than what would be in the case of a single crystalline cell. The efficiency of modules produced using this technology ranges from 11%-14% [2].

2.1.3 Thin Film PV technologies

Thin film PV cells are manufactured through the deposition of several thin layers of atoms or molecules of certain materials on a holding surface. They have the advantage over their crystalline Silicon counterparts in their thickness and weight. They can be 1 to 10 micrometers thin as compared to 300 micrometers for Silicon cells [5]. Another advantage is that they can be manufactured using an automated large area process that further reduces their cost. Thin film PV cells do not employ the metal grid required for carrying current outside the cell. However, they make use of a thin layer of conducting oxides to carry the output current to the external circuit. The electric field in the p-n junction of the cell is created between the surface contacts of two different materials, creating what is called a heterojunction PV cell. Thin film PV can be integrated on windows and facades of buildings because they generate electricity while allowing some light to pass through. Two common thin film materials are Copper indium diselenide (CIS for short) and Cadmium Telluride (CdTe). CIS thin films are characterized by their very high absorptivity. PV cells that are built from this material are of the heterojunction type. The top layer can be cadmium sulfide, while the bottom layer can be gallium to improve the efficiency of the device. Cadmium Telluride PV cells are similar to CIS in their construction and manufacturing process. However, the resistivity of p-type CdTe is quite high therefore increasing the internal losses. This issue can be addressed through the use of intrinsic CdTe while using a layer of zinc telluride between the cell and the back contacts. Efficiency for these technologies is about 10-13% [2].

2.2 Photovoltaic cell equivalent circuit model

The equivalent circuit model of a PV cell is needed in order to simulate its real behavior. One of the models proposed in literature is the double exponential model [6] depicted in figure 2-2. Using the physics of p-n junctions, a cell can be modeled as a DC current source in parallel with two diodes that represent currents escaping due to diffusion and charge recombination mechanisms. Two resistances, R_s and R_p, are included to model the contact resistances and the internal PV cell resistance respectively. The values of these two resistances can be obtained from measurements or by using curve fitting methods based on the I-V characteristic of the cell. The work done in [7] is an example of using curve fitting techniques to approximate the values of R_s and R_p.

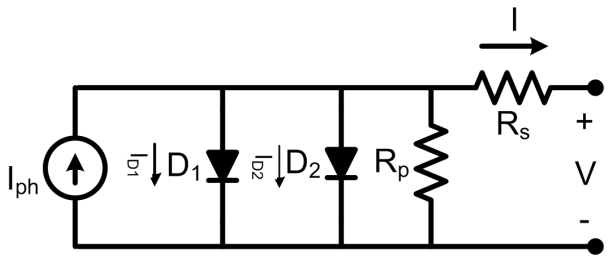

Figure 2-2: Double exponential PV cell model.

The relationship between the PV cell output current and terminal voltage is governed by:

$$
\begin{aligned}
I &= I_{ph} - I_{D1} - I_{D2} - \frac{V + IR_s}{R_p} \\
I_{D1} &= I_{01}\left[\exp\left(\frac{q(V + IR_s)}{akT}\right) - 1\right] \\
I_{D2} &= I_{02}\left[\exp\left(\frac{q(V + IR_s)}{akT}\right) - 1\right]
\end{aligned}
\tag{2.1}
$$

where I_{ph} is the PV cell internal generated photocurrent, I_{D1} and I_{D2} are the currents passing through diodes D_1 and D_2, *a* is the diode ideality factor, k is the Boltzmann constant ($1.3806503 \times 10^{-23}$ J/K),

T is the cell temperature in degrees Kelvin, *q* is the electron charge ($1.60217646 \times 10^{-19}$ C), I_{01} and I_{02} are the reverse saturation currents of each diode respectively.

Assuming that the current passing in diode D_2 due to charge recombination is small enough to be neglected, a simplified PV cell model can be reached as shown in figure 2-3.

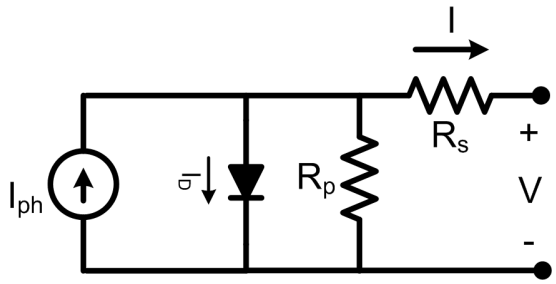

Figure 2-3: Simplified PV cell model.

This model provides a good compromise between accuracy and model complexity and has been used in several previous works [8], [9] and [10]. In this case, current I_{D2} can be omitted from (2.1) and the relation simplifies to:

$$I = I_{ph} - I_0 \left[\exp\left(\frac{q(V + IR_s)}{akT} \right) - 1 \right] - \frac{V + IR_s}{R_p} \tag{2.2}$$

It is clear that the relationship between the PV cell terminal voltage and output current is nonlinear because of the presence of the exponential term in 2.1 and 2.2. The presence of the p-n semiconductor junction is the reason behind this nonlinearity. The result is a unique I-V characteristic for the cell where the current output is constant over a wide range of voltages until it reaches a certain point where it start dropping exponentially. The I-V characteristic of a 200 W PV module by Kyocera is shown in figure 2-4. A PV module is the result of connecting several PV cells in series to order to increase the output voltage. The characteristic has the same shape except for changes in the magnitude of the open circuit voltage.

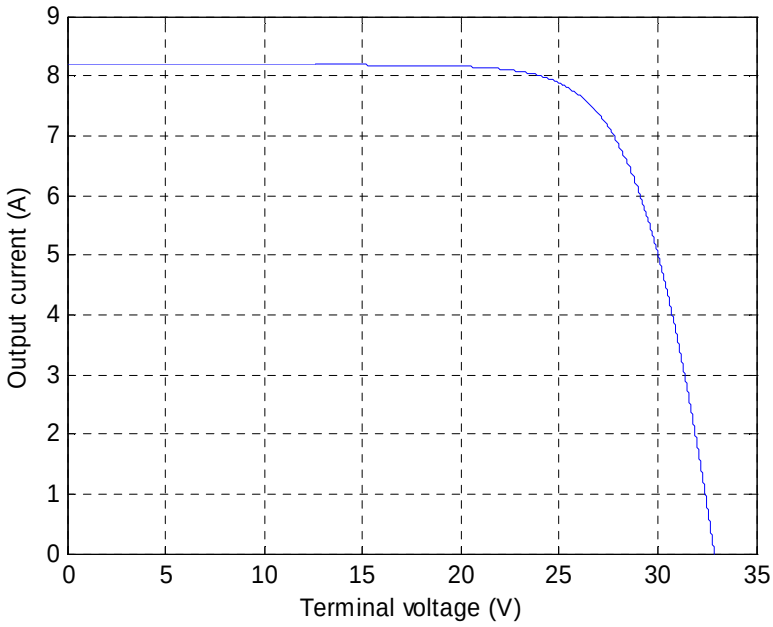

Figure 2-4: I-V characteristic of a Photovoltaic module

Another important relationship in PV cells is the power-voltage characteristic. The product of multiplying the current and voltage is evaluated at each point in the curve to find out how much power can be obtained as voltage changes. The power-voltage relationship for the PV module is depicted in figure 2-5. Initially, power starts increasing as voltage increases. A certain point in the curve is reached where maximum power output can be obtained; this point is therefore referred to as the Maximum Power Point (MPP). After this point, power starts dropping as the terminal voltage increases until it eventually reaches zero at open circuit voltage. Power output from a PV cell is dictated by the magnitude of the load resistance, defined by the division of the cell voltage overcurrent, in case of fixed loads. If the load impedance does not equal the value required to extract maximum power, then it is possible to use a switched mode DC converter to do the matching between the PV cell and the load. The process of changing the PV array terminal voltage externally to extract maximum power for different loads is known as Maximum Power Point Tracking (MPPT). Several

techniques are can be used to perform this task as will be explained in a following section of the thesis.

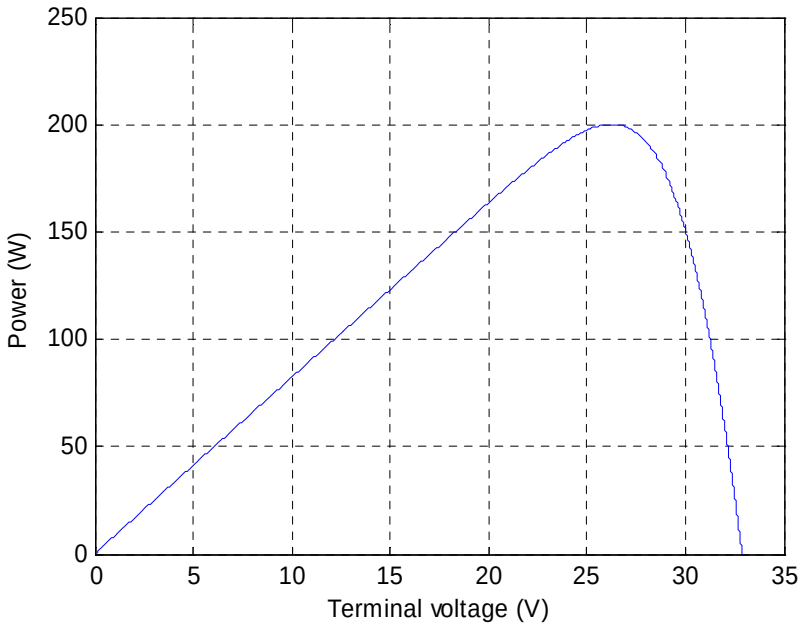

Figure 2-5: Power-Voltage relationship of a PV module

The PV cell characteristics also depend on external factors including temperature and solar irradiation level. To incorporate these effects into the model, two additional relations are used. Output current varies with solar irradiation and temperature through:

$$I = \left(I_n + K_I \Delta T\right)\frac{G}{G_n} \tag{2.3}$$

where I_n is the nominal PV cell output current (at 25 °C and 1000 W/m^2), K_I is the current/temperature variation coefficient (A/°C), ΔT is the variation from the nominal temperature (25°C) and G_n is the nominal solar irradiation (1000 W/m^2). The value of K_I is relatively small and this makes the cell output current linearly dependent on solar radiation level more than temperature.

Temperature, however, has a strong effect on the reverse saturation current, I_0 in 2.2. The following relation can be used to model that effect [7]:

$$I_0 = \frac{I_{sc,n} + K_I \Delta T}{\exp(q(V_{oc,n} + K_V \Delta T) / akT) - 1} \tag{2.4}$$

where $I_{sc,n}$ is the nominal short circuit current of the PV cell, $V_{oc,n}$ is the nominal open circuit voltage, K_I and K_V are the current and voltage temperature variation coefficients, in A/°C and V/°C, respectively.

The effect of solar irradiation and temperature on the characteristics of the PV module is depicted in figures 2-6, 2-7, 2-8 and 2-9. To investigate the effect of solar irradiation on the currents and voltages of the module, temperature was held constant at 25 °C and the resulting I-V and P-V characteristics were plotted. Figure 2-6 shows the I-V characteristics of the module at different irradiation levels of 500, 800 and 1000 W/m^2. The P-V characteristics are shown in figure 2-7 for the same irradiation levels mentioned. It is noticed that output current is directly proportional to changes in solar irradiation as expected from the model. Maximum output power of the module is reduced by half when the solar irradiation drops to 500 W/m^2. However, the open circuit voltage does not change significantly. To find out the effect of temperature on the module performance, solar irradiation level was assumed constant at 1000 W/m^2 while allowing temperature to vary between 25 and 80 °C. The result is shown in figures 2-8 and 2-9 for the I-V and P-V characteristics as temperature was set to 25, 60 and 80 °C respectively. The open circuit voltage of the module decreases as surface temperature increases. Current, on the other hand, increases slightly with temperature. The maximum power output of the module reduces as the surface temperature rises.

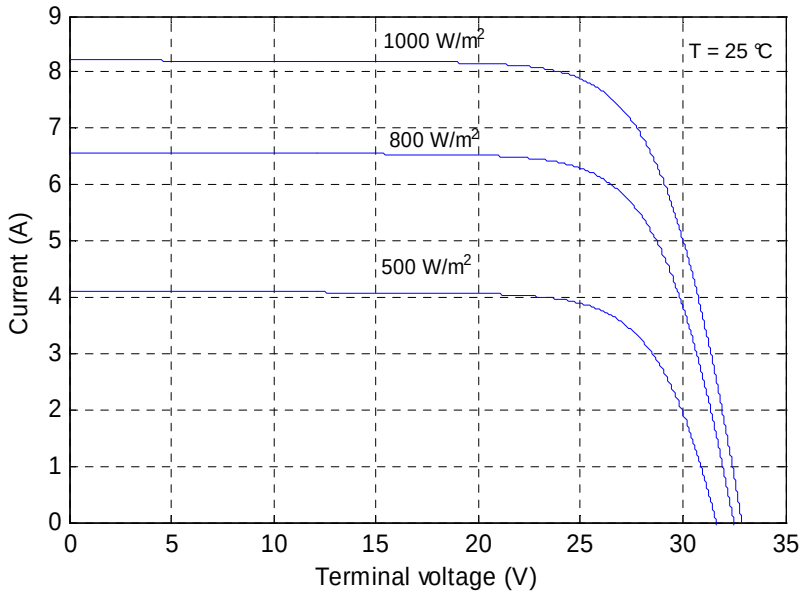

Figure 2-6: I-V characteristics of the PV module under different solar irradiation levels

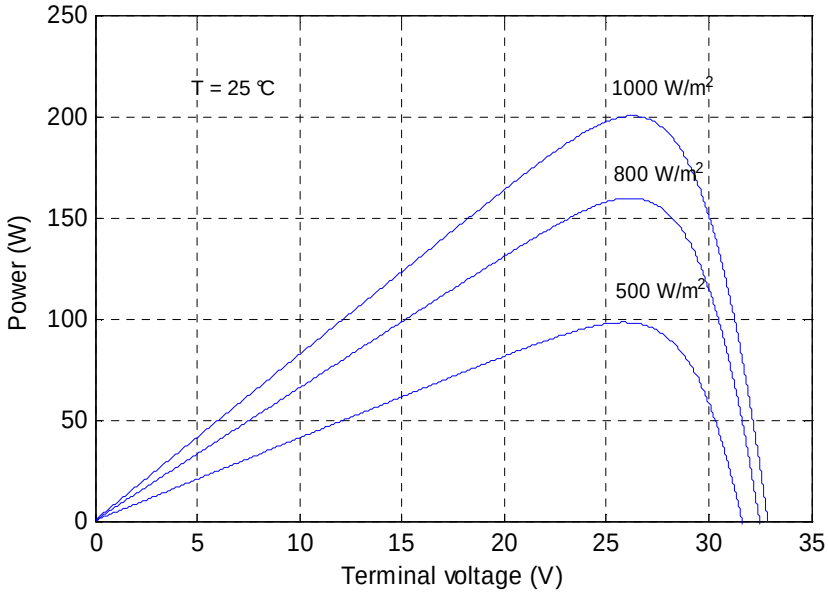

Figure 2-7: P-V characteristics of the PV module under different solar irradiation levels

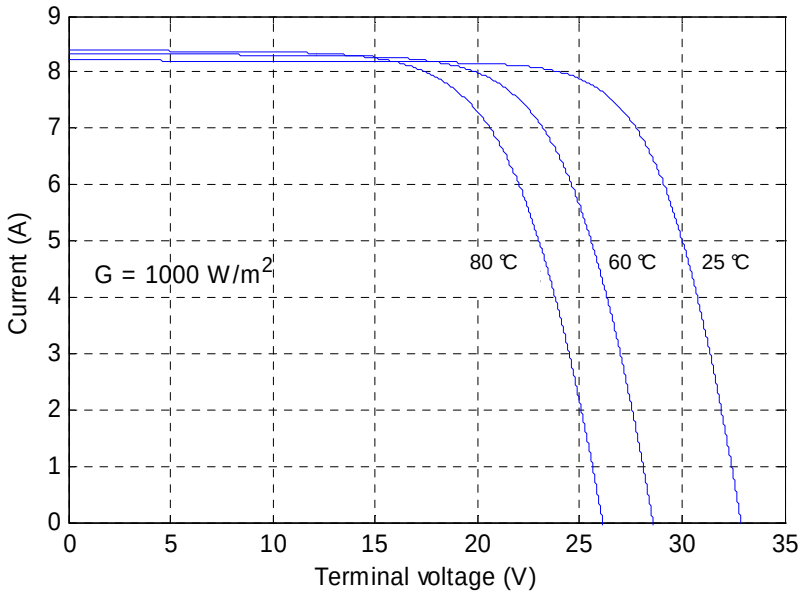

Figure 2-8: I-V characteristics of the PV module at different surface temperatures

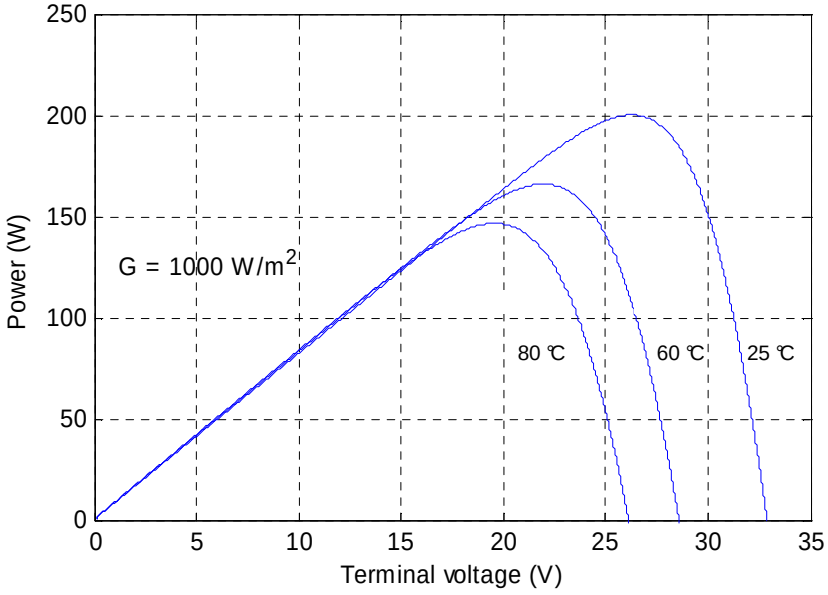

Figure 2-9: P-V characteristics of the PV module at different surface temperatures

2.3 Switched mode DC-DC converters

DC/DC converters are used in a wide variety of applications including power supplies, where the output voltage should be regulated at a constant value from a fluctuating power source, to reduce the ripples in the output voltage or achieve multiple voltage levels from the same input voltage. Several topologies exist to either increase or decrease the input voltage or perform both functions together using a single circuit. The three basic topologies of DC converters are: buck (step down), boost (step up) and the buck-boost converter topologies.

2.3.1 Buck Converter

The schematic diagram of a buck DC converter is shown in figure 2-10. It is composed of two main parts: a DC chopper and an output LC filter to reduce the ripples in the resulting output. The output voltage of the converter is less than the input as determined by the duration the semiconductor switch *Q* is closed. Under continuous conduction mode (CCM), the current I_L passing through the inductor does not reach zero. The time integral of the inductor voltage over one period in steady state is equal to zero. From that, the relation between the input and output voltages can be obtained:

$$(V_{in} - V_{out})\,t_{on} - V_{out}\,t_{off} = 0$$
$$\frac{V_{out}}{V_{in}} = \frac{t_{on}}{t_{on} + t_{off}} = d \qquad where \quad d = duty\ cycle \tag{2.5}$$

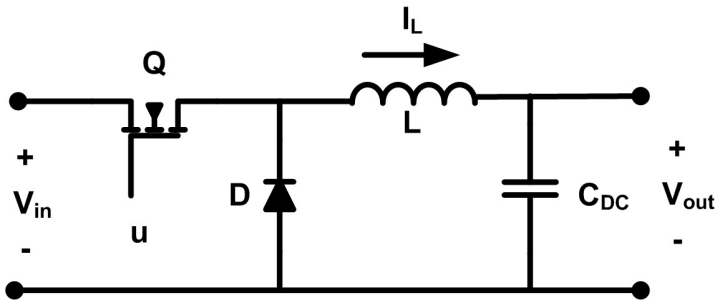

Figure 2-10: Schematic diagram of a buck DC converter

2.3.2 Boost Converter

The boost DC converter is used to step up the input voltage by storing energy in an inductor for a certain time period, and then uses this energy to boost the input voltage to a higher value. The circuit diagram for a boost converter is shown in figure 2-11. When switch *Q* is closed, the input source charges up the inductor while diode *D* is reverse biased to provide isolation between the input and the output of the converter. When the switch is opened, energy stored in the inductor and the power supply is transferred to the load. The relationship between the input and output voltages is given by:

$$V_{in}t_{on} + (V_{in} - V_{out})t_{off} = 0$$
$$\frac{V_{out}}{V_{in}} = \frac{t_{on} + t_{off}}{t_{off}} = \frac{1}{1-d} \tag{2.6}$$

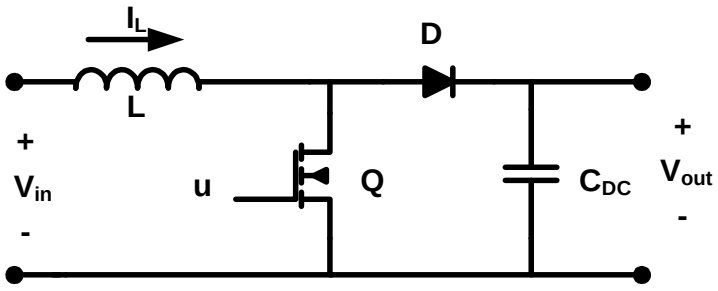

Figure 2-11: Schematic diagram of a DC boost converter.

2.3.3 Buck-Boost Converter

This converter topology can be used to perform both functions of stepping the input voltage up or down, but the polarity of the output voltage is opposite to that of the input. The input and output voltages of this configuration are related through

$$V_{in}t_{on} + V_{out}t_{off} = 0$$
$$\frac{V_{out}}{V_{in}} = \frac{-t_{on}}{t_{off}} = \frac{-d}{1-d} \tag{2.7}$$

2.4 Three phase inverters (DC-AC converters)

Voltage source inverters (VSI) are mainly used to convert a constant DC voltage into 3-phase AC voltages with variable magnitude and frequency. Figure 2-12 shows a schematic diagram of a 3 phase VSI. The inverter is composed of six switches S_1 through S_6 with each phase output connected to the middle of each "inverter leg". Two switches in each phase are used to construct one leg. The AC output voltage from the inverter is obtained by controlling the semiconductor switches ON and OFF to generate the desired output. Pulse width modulation (PWM) techniques are widely used to perform this task. In the simplest form, three reference signals are compared to a high frequency carrier waveform. The result of that comparison in each leg is used to turn the switches ON or OFF. This technique is referred to as sinusoidal pulse width modulation (SPWM). It should be noted that the switches in each leg should be operated interchangeably, in order not to cause a short circuit of the DC supply.

Insulated Gate Bipolar Transistors (IGBTs) and power MOSFET devices can be used to implement the switches. Each device varies in its power ratings and switching speed. IGBTs are well suited for applications that require medium power and switching frequency [11].

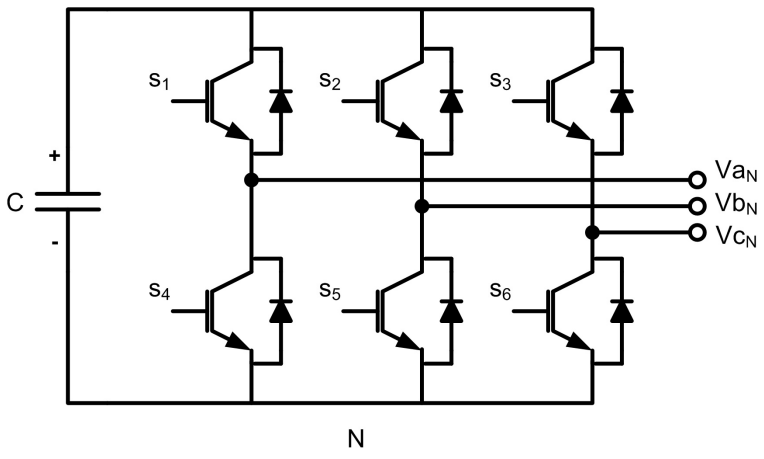

Figure 2-12: Three phase voltage source inverter (VSI)

2.5 Maximum Power Point Tracking (MPPT) Techniques

MPPT techniques are used to control DC converters in order to extract maximum output power from a PV array under a given weather condition. The DC converter is continuously controlled to operate the array at its maximum power point despite possible changes in the load impedance. Several techniques have been proposed in literature to perform this task.

2.5.1 Perturb and Observe

The perturb and observe algorithm is a simple technique for maximum power point tracking. It is based on controlling the duty cycle (d) of a DC-DC converter to adjust the PV array terminal voltage at the maximum power point [12]. The power output of the array is monitored every cycle and is compared to its value before each perturbation is made. If a change (either positive or negative) in the duty cycle of the DC-DC converter causes output power to increase, the duty cycle is changed in the same direction. If it causes the output power to decrease, then it is reversed to the opposite direction. The algorithm is represented in figure 2-13.

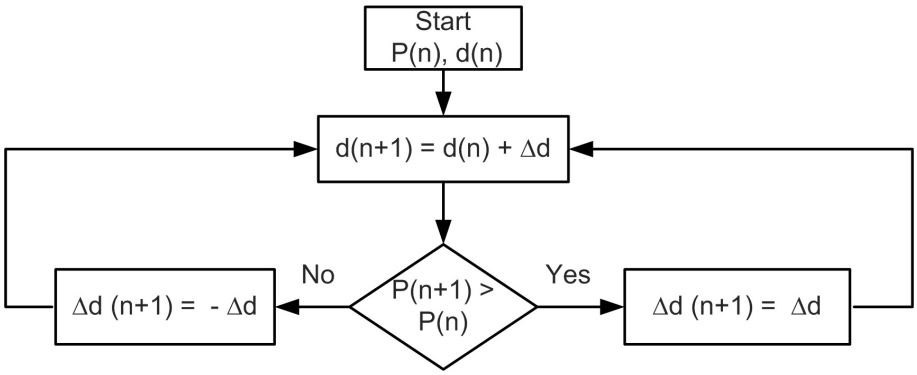

Figure 2-13: Flowchart of the perturb and observe algorithm

The performance of the algorithm is affected by the choice of the perturbation magnitude (*Δd*) of the converter switching duty cycle. Large perturbations cause large output power fluctuations around the MPP while small perturbations slow down the algorithm. Modifications to this technique are

published in [13], [14] and [15] to improve performance while maintaining the basic principle of operation. Table 2-1 illustrates the operation sequence of the algorithm.

Table 2-1: Perturbation directions for the P&O algorithm based on output power variations

Change in duty cycle, Δd	Effect on output power	Next perturbation, Δd (n+1)
Increase	Increase	Increase
Increase	Decrease	Decrease
Decrease	Increase	Decrease
Decrease	Decrease	Increase

2.5.2 Incremental Conductance

This algorithm exploits the fact that the slope of the power-voltage curve of a PV array is equal to zero at the maximum power point, as shown in figure 2-5. The slope is positive in the area to the left of the maximum power point and negative in the area to the right. Mathematically, this can be summarized as:

$$\begin{aligned} dP/dV &= 0, \quad at\ MPP \\ dP/dV &> 0, \quad left\ of\ MPP \\ dP/dV &< 0, \quad right\ of\ MPP \end{aligned} \tag{2.8}$$

This can be simplified using the following approximation:

$$dP/dV = d(IV)/dV = I + V\,dI/dV \approx I + V\,\Delta I/\Delta V \tag{2.9}$$

From that, (2.8) can be rewritten as:

$$\begin{aligned} \Delta I/\Delta V &= -I/V, \quad at\ MPP \\ \Delta I/\Delta V &> -I/V, \quad left\ of\ MPP \\ \Delta I/\Delta V &< -I/V, \quad right\ of\ MPP \end{aligned} \tag{2.10}$$

The incremental conductance algorithm is illustrated in figure 2-14 where V_{ref} is used as a reference control signal for the DC converter [12], [16], [17]. Similar to the P&O algorithm, the performance of the incremental conductance MPPT is affected by the increment size of V_{ref}, used here as the control variable.

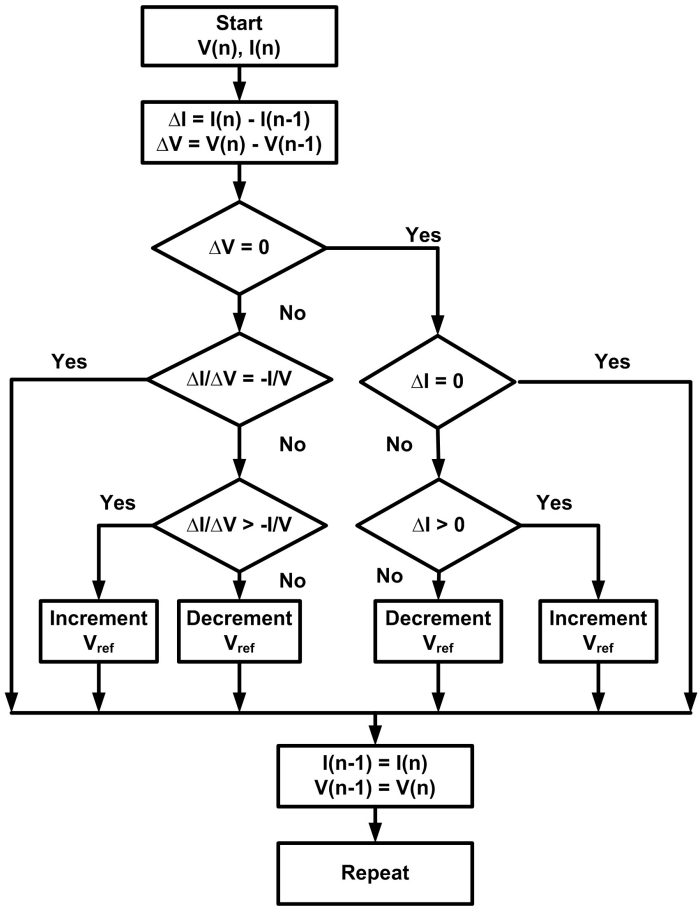

Figure 2-14: Flowchart of the Incremental conductance MPPT algorithm [12]

2.5.3 Fuzzy logic-based MPPT

Fuzzy logic MPPT control is divided into three stages: fuzzification, rule based table look-up and defuzzification. During the fuzzification process, control variable are converted from a numerical value to a linguistic representation like Positive Big (*PB*), Positive Small (*PS*), Zero (*Z*), Negative

Small (*NS*) and Negative Big (*NB*). The slope of the P-V curve (S) and the change of slope (ΔS) were used in [18] as the input control variables to the fuzzification stage.

$$S = \frac{P(n+1) - P(n)}{V(n+1) - V(n)}$$
$$\Delta S = S(n+1) - S(n) \tag{2.11}$$

where *n* is the sampling interval, *V* and *P* are the terminal voltage and output power of the PV array respectively. Next, a look-up table is used to determine the control action of the converter duty cycle based on the linguistic magnitude of the variables. If the PV array is connected to a boost DC-DC converter, then table 2-2 can be used to issue the control decisions [19]. The look up table is dependent on the DC converter topology being used. Since the control command is also in linguistic format, it should be first converted to a numerical value during the defuzzification stage. When both the slope and change of slope variables reach zero, the maximum power point is reached.

Fuzzy logic controllers can perform maximum power point tracking effectively under changing weather conditions. However, there is some difficulty designing the look up table and the rules that govern the operation of the controller for different converter topologies. In addition, thresholds that define the linguistic variables are to be carefully selected because they can impact the algorithm performance. An adaptive fuzzy logic controller was proposed in [20] to dynamically tune these thresholds to achieve improved performance.

Table 2-2: Rule based look-up table for fuzzy logic MPPT [19]

S \ ΔS	*NB*	*NS*	*Z*	*PS*	*PB*
NB	Z	Z	NB	NB	NB
NS	Z	Z	NS	NS	NS
Z	NS	Z	Z	Z	PS
PS	PS	PS	PS	Z	Z
PB	PB	PB	PB	Z	Z

2.5.4 Neural networks

Neural networks based MPPT is one of the techniques suited for implementation using microcontrollers [21], [22]. A neural network is composed of three layers: the input, hidden and output layers. Inputs to a network can be the array terminal voltage and the solar irradiation level or any other measurements needed by the MPPT algorithm. Each node in the network is referred to as a neuron; these neurons are connected together through lines that are associated with certain weighted sums w_{ij}. The effectiveness of this MPPT technique is mainly determined by the hidden layer and the amount of training the network received. The training process might span several months or years where the network is subjected to various measurements obtained from the PV system. Using this information, the weights between the neurons are tuned to generate the required output which could be a command to change a DC converter duty cycle. A disadvantage of this technique is the lengthy training process it needs before the neural network can accurately track the maximum power point, in addition to its dependency on the characteristics of the PV array to which it is connected.

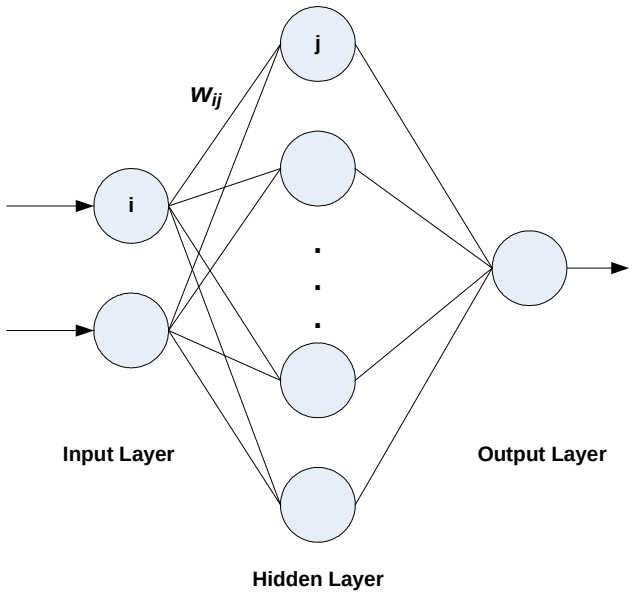

Figure 2-15: Neural network for MPPT control

Chapter 3
Control of Three Phase Grid Connected PV System

This chapter covers the control system developed to operate a grid connected PV system. First, the structure of the system and its control blocks are introduced. Then, the function of each block is examined in detail. An overview of the dq transformation and sinusoidal PWM technique are presented for their importance in building the inverter control system. The boost DC converter is controlled using an open loop maximum power point tracking technique in order to achieve fast control response to transients and changes in weather conditions. The control system is assessed based on: the quality of the injected AC current into the grid, as determined by the Total Harmonic Current Distortion (THDI) limits specified by the IEEE Std. 929-2000; and the speed of the control system in tracking the maximum power point as weather conditions, mainly solar irradiation, change. The system was studied under grid-side fault conditions to examine the effect of the transformer topology selection on the propagation of zero sequence currents to the grid. These currents can intervene with the correct operation of the utility protection relays.

3.1 System structure

The PV system under study is shown in figure 3-1. A photovoltaic array is used to convert sunlight into DC current. The output of the array is connected to a boost DC converter that is used to perform MPPT functions and increase the array terminal voltage to a higher value so it can be interfaced to the distribution system grid at 6.6 kV. The DC converter controller is used to perform these two functions. A DC link capacitor is used after the DC converter and acts as a temporary power storage device to provide the voltage source inverter with a steady flow of power. The capacitor's voltage is regulated using a DC link controller that balances input and output powers of the capacitor. The voltage source inverter is controlled in the rotating *dq* frame to inject a controllable three phase AC

current into the grid. To achieve unity power factor operation, current is injected in phase with the grid voltage. A phase locked loop (PLL) is used to lock on the grid frequency and provide a stable reference synchronization signal for the inverter control system, which works to minimize the error between the actual injected current and the reference current obtained from the DC link controller. An adjustable speed drive (ASD) and an RL load are connected to the grid to simulate some of the loads that are connected to a distribution system network. An LC low pass filter is connected at the output of the inverter to attenuate high frequency harmonics and prevent them from propagating into the power system grid. A second order LCL filter is obtained if the leakage inductance of the interfacing transformer is referred to the low voltage side. This provides a smooth output current which is low in harmonic content.

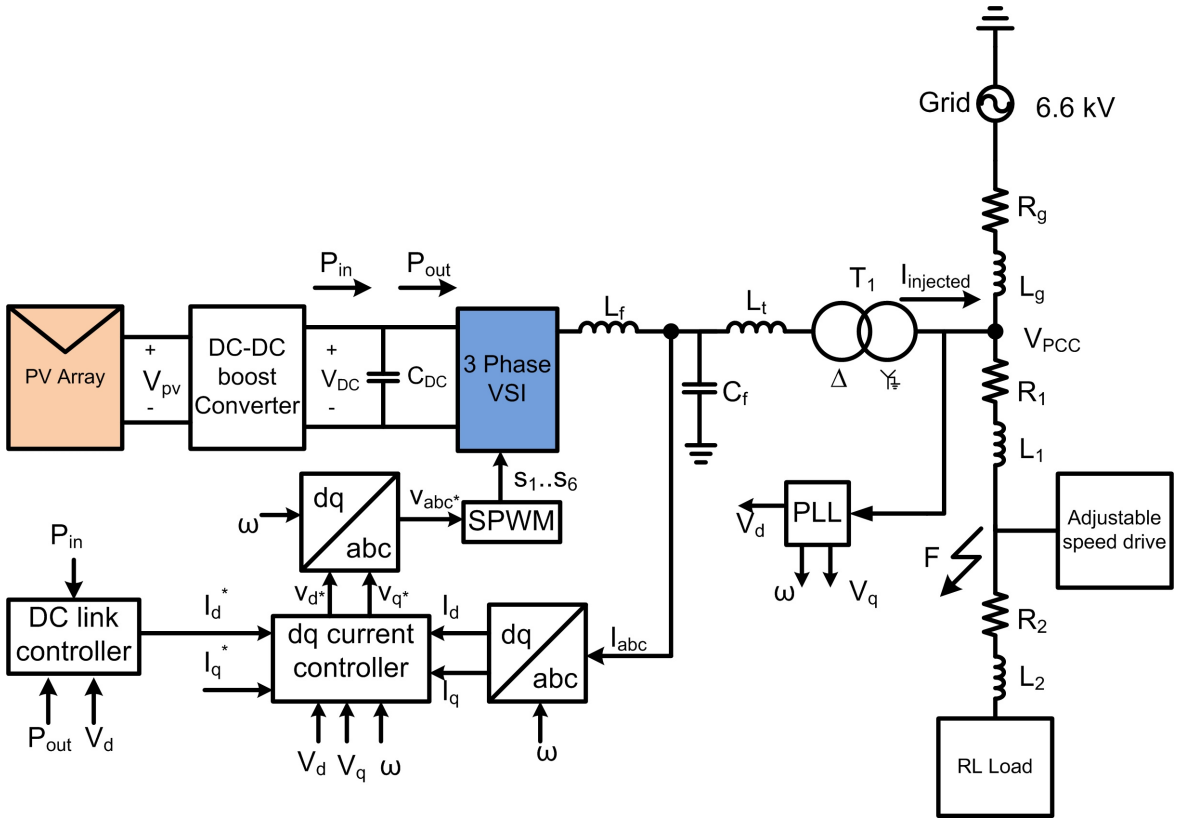

Figure 3-1: Grid connected PV system structure

3.2 The *abc/dq* Transformation

The *dq* transformation is used to transform three phase system quantities like voltages and currents from the synchronous reference frame (*abc*) to a synchronously rotating reference frame with three constant components when the system is balanced. The relationship that govern the transformation from the *abc* to *dq* frame is

$$\begin{bmatrix} x_d \\ x_q \\ x_0 \end{bmatrix} = T \times \begin{bmatrix} x_a \\ x_b \\ x_c \end{bmatrix}$$
$$T = \sqrt{\frac{2}{3}} \times \begin{bmatrix} \cos(\omega t) & \cos(\omega t - 2\pi/3) & \cos(\omega t + 2\pi/3) \\ -\sin(\omega t) & -\sin(\omega t - 2\pi/3) & -\sin(\omega t + 2\pi/3) \\ 1/\sqrt{2} & 1/\sqrt{2} & 1/\sqrt{2} \end{bmatrix} \tag{3.1}$$

where x can be either a set of three phase voltages or currents to be transformed, T is the transformation matrix and ω is the angular rotation frequency of the frame [23]. The angle between the direct axis (d-axis) and phase a-axis is defined as θ as shown in figure 3-2.

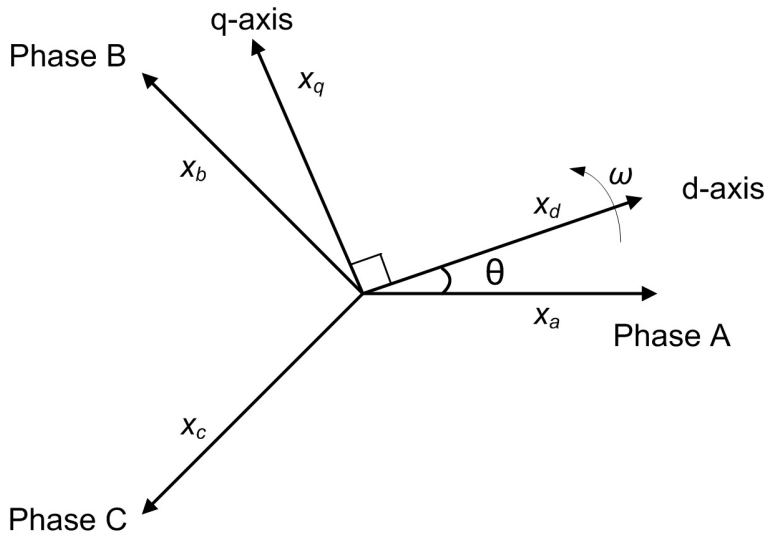

Figure 3-2: Relationship between the abc and dq reference frames

The result of this transformation is three constant rotating components: the direct (d), quadrature (q) and zero (0) components. In balanced three phase systems, the zero component can be ignored since

$$x_a + x_b + x_c = 0 \tag{3.2}$$

The inverse transformation from the *dq* frame to the *abc* frame can be obtained by applying

$$\begin{bmatrix} x_a \\ x_b \\ x_c \end{bmatrix} = T^{-1} \times \begin{bmatrix} x_d \\ x_q \\ x_0 \end{bmatrix}$$
$$T^{-1} = \sqrt{\frac{2}{3}} \times \begin{bmatrix} \cos(\omega t) & -\sin(\omega t) & 1/\sqrt{2} \\ \cos(\omega t - 2\pi/3) & -\sin(\omega t - 2\pi/3) & 1/\sqrt{2} \\ \cos(\omega t + 2\pi/3) & -\sin(\omega t + 2\pi/3) & 1/\sqrt{2} \end{bmatrix} \tag{3.3}$$

This transformation is useful in developing the control system for the voltage source inverter under current control to regulate the output of the PV system. Active and reactive powers injected from the PV system can be calculated using the following relationships

$$\begin{aligned} P &= V_d I_{d,injected} + V_q I_{q,injected} \\ Q &= -V_d I_{q,injected} + V_q I_{d,injected} \end{aligned} \tag{3.4}$$

where V_d, V_q are the *dq* voltages at PCC at the grid side of the transformer, $I_{d,injected}$ and $I_{q,injected}$ are the *dq* components of the injected current at the grid side. It is evident that in the computation of reactive power *Q*, there is cross coupling between the direct and quadrature current and voltage components. This can be eliminated through the use of a phase locked loop (PLL) that locks on the grid frequency in such a way that the quadrature component of the voltage at the point of PV system connection is forced to zero. In this case, equation 3.4 simplifies to

$$\begin{aligned} P &= V_d I_{d,injected} \\ Q &= -V_d I_{q,injected} \end{aligned} \tag{3.5}$$

This means that the direct and quadrature components of the inverter output current can be used to control the active and reactive output powers from the PV array system, as they are related to the injected currents by the transformer turns ratio. This is based on the assumption that the voltage at the point of common coupling (PCC) is relatively constant. In current practice, distribution systems have regulation mechanisms to keep voltage within specified limits.

3.3 Phase Locked Loop (PLL)

The role of the phase locked loop is to provide the rotation frequency, direct and quadrature voltage components at the point of common coupling (PCC) by resolving the grid voltage *abc* components. Multiple control blocks of the PV system rely on this information to regulate their output command signals. As stated earlier, the PLL computes the rotation frequency of the grid voltage vector by first transforming it to the *dq* frame, and then force the quadrature component of the voltage to zero to eliminate cross coupling in the active and reactive power terms [23]. A proportional-integral controller is used to perform this task as shown in figure 3-3. The proportional (K_p) and integral (K_i) gains of the controller were set through an iterative process to achieve a fast settling time.

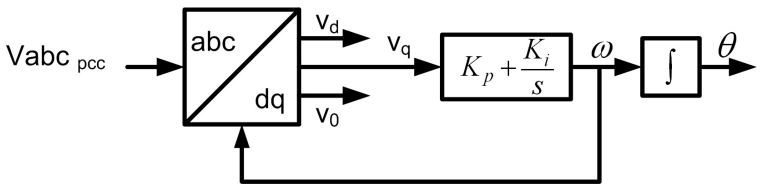

Figure 3-3: Schematic diagram of the phase locked loop (PLL)

The output from the PI controller is the rotation frequency ω in rad/s. Integrating this term results in the rotation angle θ in radians. The operation of the PLL is governed by

$$\begin{aligned} \omega &= K_P V_q + K_I \int V_q \, dt \\ \theta &= \int \omega \, dt \end{aligned} \tag{3.6}$$

3.4 Open loop MPPT using a boost DC converter

Grid connected PV systems are subject to fast dynamics in the power system as opposed to those connected to fixed loads. A fast MPPT technique is needed to help extract power under those conditions. There are several techniques in literature that could quickly locate the maximum power point of a PV array including those based on Fuzzy logic and neural networks. However, they are difficult to implement and depend on the characteristics of the PV system. Perturb and observe and incremental conductance techniques do not suffer from the aforementioned problems, but they have a slower response to weather changes. From that, it is necessary to develop an MPPT technique that is a good compromise between these two types. The open loop MPPT technique used here tries to eliminate the computational overhead associated with the feedback action in present algorithms, without compromising the correct operation of the array.

The method proposed here treats the voltage at the maximum power point as a fraction of the PV array open circuit voltage. From several PV cell manufacturers' datasheets, the fraction (C_f) is estimated to be in the range from 0.77 to 0.8. The relationship is dictated by:

$$V_{MP} = C_f \times V_{OC} \tag{3.7}$$

The determination of the maximum power point in this case requires measuring the array open circuit voltage and multiplying it by a constant. A disconnection of the PV array from the system is needed to obtain that measurement. To get around this difficulty, separate PV cells can be installed within the array and their open circuit voltage can be measured in order to estimate the array voltage. These cells will be subjected to the same solar radiation and surface temperature levels and thus will allow for a very good estimate of V_{OC}. With this concept in mind, the speed of open loop control can be exploited without the need for measuring the output power of the PV array in every control cycle. After finding a value for V_{MP}, the DC-DC boost converter is used to force the array voltage to follow it. This offers

improved dynamic and steady state response during the presence of quick variations in the power system or solar radiation level. A separate controller is dedicated for controlling the capacitor voltage to match power going into it from the PV array, and power going out to the grid.

The DC converter regulates the PV array voltage by continuously switching on and off at high frequency. The current I_L that goes through the inductor in figure 3-4 is the same as the current output of the PV array. When the DC converter switch is turned on, the inductor starts charging and current I_L increases. Assuming the voltage drop across the switch is negligible, the PV array voltage is related to the inductor current through the following relationship:

$$V_{PV} = L\frac{dI_L}{dt} \tag{3.8}$$

As the inductor current reaches steady state, the rate of change of current (dI_L/dt) decreases and this causes the PV array terminal voltage to decrease and move down the voltage-power curve as shown in figure 3-4 (a). If the switch is closed long enough, the PV array voltage will eventually drop to zero and the inductor will have the PV array short circuit current passing through it.

When the switch is turned off, the inductor and the PV array will start supplying current to the DC-link capacitor. This causes the inductor to discharge and its current decreases with time. The direction along the PV array voltage-power curve is reversed and voltage will start moving towards V_{OC} as shown in figure 3-4 (b). By quickly switching the DC converter on and off around the maximum power point, the PV array will output maximum power at a given solar irradiation and temperature levels. The switching function that governs the DC converter operation is:

$$u = \begin{cases} 1 & V_{PV} - V_{mp} > 0 \\ 0 & V_{PV} - V_{mp} < 0 \end{cases} \tag{3.9}$$

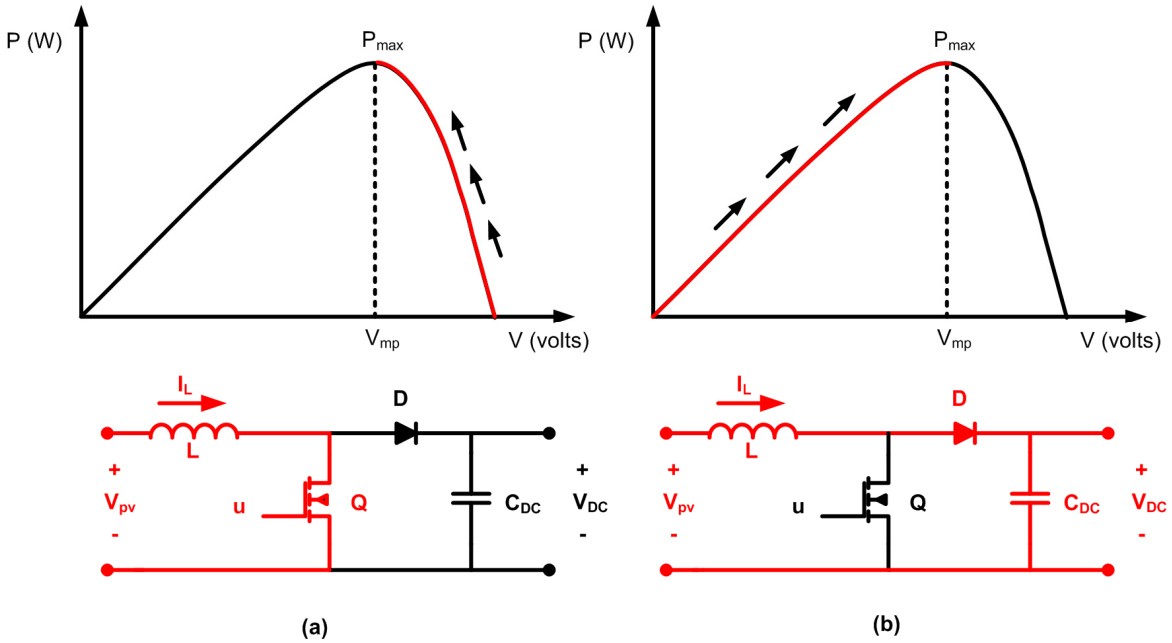

Figure 3-4: Output power from the PV array when the converter switch is (a) ON and (b) OFF

The PV array voltage will slide along the curve following the direction dictated by the switching signal. Implementation of the switching function can be achieved using a comparator circuit that triggers when the instantaneous PV array voltage exceeds the maximum power point. After the DC converter switch turns on, the array operating voltage will move back to the maximum power point as in figure 3-4 (a). If the PV array voltage drops below the maximum power point, the switch is turned off to allow the inductor to discharge power to the DC link capacitor and allow the array voltage to return to the MPP as in figure 3-4 (b). A simple comparator circuit can be realized using an op amp as shown in figure 3-5.

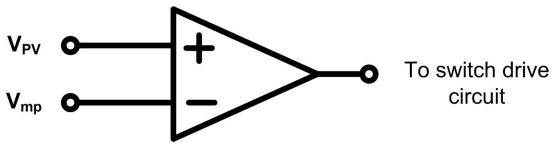

Figure 3-5: comparator circuit

3.5 Modeling and Control of the Three phase VSI in the *dq* frame

The state equations describing the dynamics of the output currents and voltages of the voltage source inverter are derived in this section. The time derivatives of the inverter output current and voltage are

$$L_f \frac{d}{dt} I_{inv} = V_{inv} - V_C \tag{3.10}$$

$$C_f \frac{d}{dt} V_C = I_{inv} - I_G \tag{3.11}$$

where L_f and C_f are the filter's inductance and capacitance respectively, V_c is the capacitor voltage and I_G is the current injected into the grid as shown in figure 3-6. Equations 3.10 and 3.11 are in matrix format where

$$I_{inv} = \begin{bmatrix} I_{inv,a} & I_{inv,b} & I_{inv,c} \end{bmatrix}^T, \quad V_C = \begin{bmatrix} V_{Ca} & V_{Cb} & V_{Cc} \end{bmatrix}^T$$

$$L_f = \begin{bmatrix} L_f & 0 & 0 \\ 0 & L_f & 0 \\ 0 & 0 & L_f \end{bmatrix}, \quad C_f = \begin{bmatrix} C_f & 0 & 0 \\ 0 & C_f & 0 \\ 0 & 0 & C_f \end{bmatrix} \tag{3.12}$$

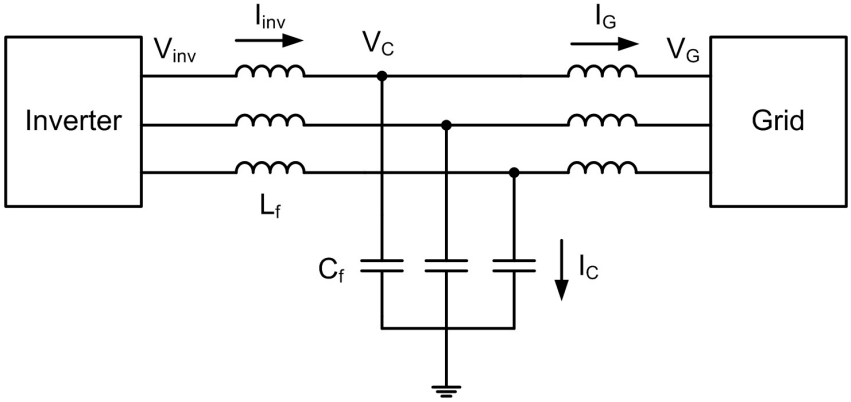

Figure 3-6: circuit diagram of a three phase grid connected inverter

Multiplying both sides of equation 3.10 by the transformation matrix *T* in 3.1, the VSI model in the *dq* frame can be obtained [24]. The following procedure is adopted to find the result of the transformation

$$\begin{aligned} TL_f \frac{d}{dt} I_{abc} &= T(V_{inv} - V_C) \\ TL_f \frac{d}{dt} T^{-1} \hat{I}_{inv} &= T(V_{inv} - V_C) \\ TL_f \hat{I}_{inv} \frac{d}{dt} T^{-1} + TL_f T^{-1} \frac{d}{dt} \hat{I}_{inv} &= \hat{V}_{inv} - \hat{V}_C \end{aligned} \tag{3.13}$$

where (^) is used to denote *dq* quantities. The previous steps use the relationship governing the inverse transformation, which is

$$I_{abc} = T^{-1} I_{dqo} \tag{3.14}$$

As a result, 3.10 becomes

$$\begin{bmatrix} 0 & \omega L_f & 0 \\ -\omega L_f & 0 & 0 \\ 0 & 0 & 0 \end{bmatrix} \hat{I}_{inv} + L_f \frac{d}{dt} \hat{I}_{inv} = \begin{bmatrix} 1 & 0 & 0 \\ 0 & 1 & 0 \\ 0 & 0 & 0 \end{bmatrix} (\hat{V}_{inv} - \hat{V}_C) \tag{3.15}$$

Since the 0-component is not contributing to both sides of the equation, it can be omitted and 3.15 can be written as

$$\begin{bmatrix} \dot{I}_{inv,d} \\ \dot{I}_{inv,q} \end{bmatrix} = \begin{bmatrix} 0 & -\omega \\ \omega & 0 \end{bmatrix} \begin{bmatrix} I_{inv,d} \\ I_{inv,q} \end{bmatrix} + \begin{bmatrix} 1/L_f & 0 \\ 0 & 1/L_f \end{bmatrix} \begin{bmatrix} V_{inv,d} \\ V_{inv,q} \end{bmatrix} - \begin{bmatrix} 1/L_f & 0 \\ 0 & 1/L_f \end{bmatrix} \begin{bmatrix} V_{Cd} \\ V_{Cq} \end{bmatrix} \tag{3.16}$$

This represents the state equation of the inverter output current in the dq frame. Applying the same procedure on 3.11, the state equation for the capacitor voltage is

$$\begin{bmatrix} \dot{V}_{Cd} \\ \dot{V}_{Cq} \end{bmatrix} = \begin{bmatrix} 0 & \omega \\ -\omega & 0 \end{bmatrix} \begin{bmatrix} V_{Cd} \\ V_{Cq} \end{bmatrix} + \begin{bmatrix} 1/C_f & 0 \\ 0 & 1/C_f \end{bmatrix} \begin{bmatrix} I_{Ld} \\ I_{Lq} \end{bmatrix} - \begin{bmatrix} 1/C_f & 0 \\ 0 & 1/C_f \end{bmatrix} \begin{bmatrix} I_{Gd} \\ I_{Gq} \end{bmatrix} \tag{3.17}$$

The output current from the VSI is regulated using proportional-integral controllers to force the error signal in each dq-component to zero. The error signal is defined as the difference between the measured output current and the reference current. The following control laws generate the required command voltages at the inverter output such that the error in the output current is minimized [32]

$$\begin{aligned} v_d^* &= K_P\left(I_d^* - I_d\right) + K_I\int\left(I_d^* - I_d\right)dt - \omega L_f I_q + V_{Gd} \\ v_q^* &= K_P\left(I_q^* - I_q\right) + K_I\int\left(I_q^* - I_q\right)dt + \omega L_f I_d + V_{Gq} \end{aligned} \tag{3.18}$$

where I_d^* and I_q^* are the dq reference currents, V_{Gd} and V_{Gq} are the dq voltages at the point of common coupling. The command voltages, v_d^* and v_q^*, are transformed back to the natural frame to be sent to the sinusoidal PWM block to generate the switching signals for the inverter.

Under unity power factor operation, the PV system injects real power only into the grid. In that case, reactive power injection is forced to zero by setting the reference current I_q^* to zero according to (3.5). The real power injection is controlled by I_d^* which is extracted from the power mismatch of the DC link capacitor. The capacitor voltage changes according to the following relation

$$\frac{d}{dt}V_{DC}^2 = \frac{2}{C}\left(P_{in} - P_{out}\right) \tag{3.19}$$

where P_{in} is the input power to the capacitor coming from the DC converter, P_{out} is the output power going to the inverter and then to the grid ignoring power losses, and C is the capacitance of the DC link. To keep the voltage constant, it is necessary to balance P_{in} and P_{out}. Since the input power is controlled by the DC converter to be the maximum output power from the PV array, the control system of the inverter performs the task of controlling the real output power by controlling I_d^*. This is achieved by using a separate DC link voltage PI controller using

$$I_d^* = \frac{1}{V_{Gd}}\left(K_P\left(P_{in} - P_{out}\right) + K_I\int\left(P_{in} - P_{out}\right)dt\right) \tag{3.20}$$

A schematic diagram of the controller is shown in figure 3-7 below. It accepts the power mismatch of the DC link capacitor as an input, and uses a proportional integral controller to generate a power control signal necessary to drive the mismatch to zero. The power control signal is then divided by the direct component of the grid voltage to obtain the reference current I_d^*. This reference is sent to the current controllers to regulate the output current of the inverter. The PI controller had a low bandwidth due to slow variations in the DC link power and to ensure that the reference current signal does not suffer any abrupt changes.

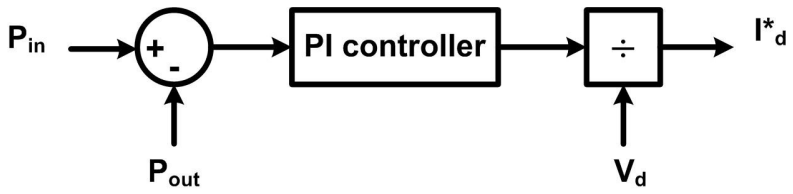

Figure 3-7: Schematic diagram of the DC link controller.

3.6 Sinusoidal Pulse Width Modulation (SPWM)

The sinusoidal pulse width modulation technique is used to control the voltage source inverter by producing the gating signals for the semiconductor switches. This technique is used to obtain three phase output voltages that can be controlled in magnitude and frequency. A reference or modulating signal is compared to a high frequency carrier signal; the result of this comparison in each phase is used to activate the switches accordingly. A separate modulating signal is used for each phase with a phase shift of 120˚ between them as shown in figure 3-8. Two important quantities in SPWM are the amplitude and frequency modulation indices, m_a and m_f respectively. The amplitude modulation index, m_a, is defined as the ratio between the amplitude of the modulating signal to the carrier signal, while the frequency modulation index, m_f, is the ratio between the frequency of the carrier signal to that of the modulating signal in 3.21 on the next page.

$$m_a = \frac{V_m}{V_{carrier}}$$
$$m_f = \frac{f_{carrier}}{f_m} \tag{3.21}$$

When the amplitude of the modulating signal is greater than that of the carrier signal, the upper switch in the corresponding phase leg in figure 2-12 is activated. This leads to the output voltage having the same magnitude of the DC link voltage. The switches in each phase leg operate in a complementary fashion in order to avoid shorting the DC kink capacitor. Figure 3-8 shows the modulating signals for a three-phase inverter and phases *A* and *B* output voltages. The line voltage between these two phases is obtained by subtracting V_b from V_a. It is clear that the output voltages need to be filtered to obtain clean sinusoidal voltages. The harmonic content in the output voltages of the inverter depends on the choice of the frequency of the carrier signal. Any even harmonics in the output line voltages in addition to harmonic orders below $m_f - 2$ will be eliminated if the following conditions hold [11]

$$m_f > 9$$
$$m_f = odd\ \ multiple\ of\ \ 3 \tag{3.22}$$

In addition to that, harmonics will be centered at m_f and its multiples 2 m_f, 3 m_f …etc., which helps ease the filtering requirements determined by the cutoff frequency. A possible choice is to have m_f = 99 which means that

$$f_{carrier} = 99 \times f_m = 99 \times 60 = 5940\,Hz$$

The magnitude of the output phase voltage (rms) can be determined using

$$V_{rms} = m_a \frac{V_{DC}}{2\sqrt{2}} \tag{3.23}$$

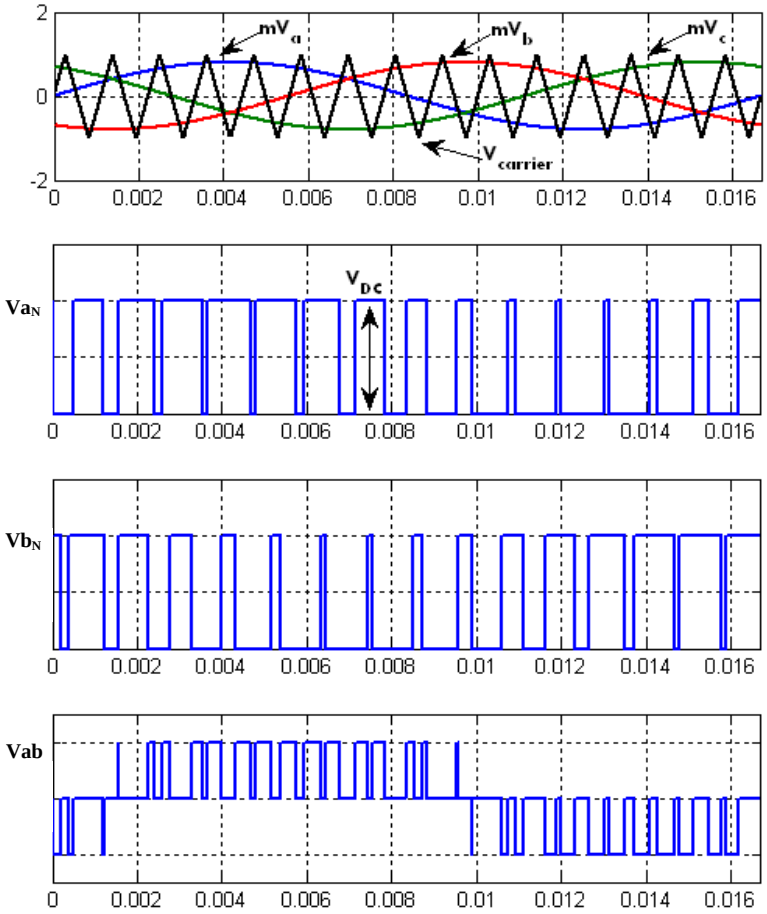

Figure 3-8: SPWM modulation signals for the VSI shown in fig 2-12

3.7 Behavior of the system during fault conditions

The operation of the distribution system protection devices can be disrupted when distributed generation (DG) sources are connected. Protection relays in radial distribution systems are set to respond to a certain magnitude of fault current, which is determined by the short circuit level at the fault location. If a DG source happens to be located between a distribution sub-station and a fault, it can contribute to the fault current. If the fault current contribution from the grid decreases, the protection relay may not be able to detect the fault and a “relay under reach” situation occurs. The situation is depicted in figure 3-9.

Most utilities require DG sources to disconnect within a few cycles of detecting a fault in the system. That might be difficult to implement especially when DG sources comprise a major part of the generated power. In Denmark for example, about 20% of the country's total electricity supply in 2007 was generated from renewable energy sources like wind turbines [25]. It is important to understand the behavior of DG sources during fault conditions and how they interact with the power system.

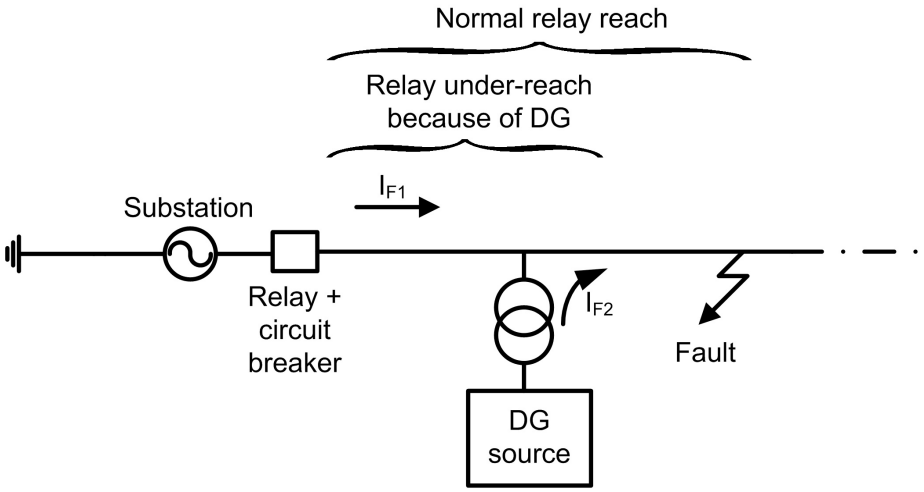

Figure 3-9: Relay under reach because of a DG source

Inverter based DG units including PV arrays do not contribute significant fault current to the system because of the presence of current limiting protection implemented in the inverter controls. This is important not to overload the power electronic switches beyond their ratings. However, the interfacing transformer between the array and the grid can play a role in the propagation of zero sequence current back to the grid. Fault current can circulate through the transformer grounding point and interact with other non-faulty phases. A simulation study was conducted in order to examine the system under these conditions.

Chapter 4
Simulation results

This chapter presents the simulation results for the grid connected PV system shown in figure 3-1 using Matlab software. The system simulation is divided into three sections: simulation of the base case under G = 1000 W/m^2 and T = 25˚C, simulation of the system when solar irradiation, G, changes from 1000 to 500 W/m^2 at T = 25˚C and finally simulation of the system during a single line to ground fault at location F (in fig 3-1).

4.1 Simulation of the PV system at G = 1000 W/m^2 and T = 25˚C

The PV system was constructed using a 100 kW array connected in centralized mode. The array composed of 25 parallel strings each containing 20 modules in series to obtain a terminal voltage suitable for grid connection purposes. To simulate the control system and the resulting output currents and voltages of the VSI, the array was subjected to a 1000 W/m^2 of solar irradiation and a temperature of 25° C. The DC output current and terminal voltage of the array were monitored during simulation to determine the current operating conditions at the specified atmospheric conditions. These two quantities are shown in figure 4-1 (a) and (b) respectively. The switching action of the DC converter caused some ripple in the output current with an average value of about 190 A, the ripple magnitude can be reduced by increasing the size of the inductor used in the boost converter. There are some initial transients in the current waveform at the beginning of simulation as the system started operation and the DC converter drove the array to the estimated maximum power point. The array terminal voltage also suffered initially from these transients. The array voltage stabilized at 526 V estimated by measuring the test cells voltages. Error during the estimation process may result due to the fact that actual voltages of the array modules might vary slightly from the theoretical value. This error can be adjusted by taking that fact into account.

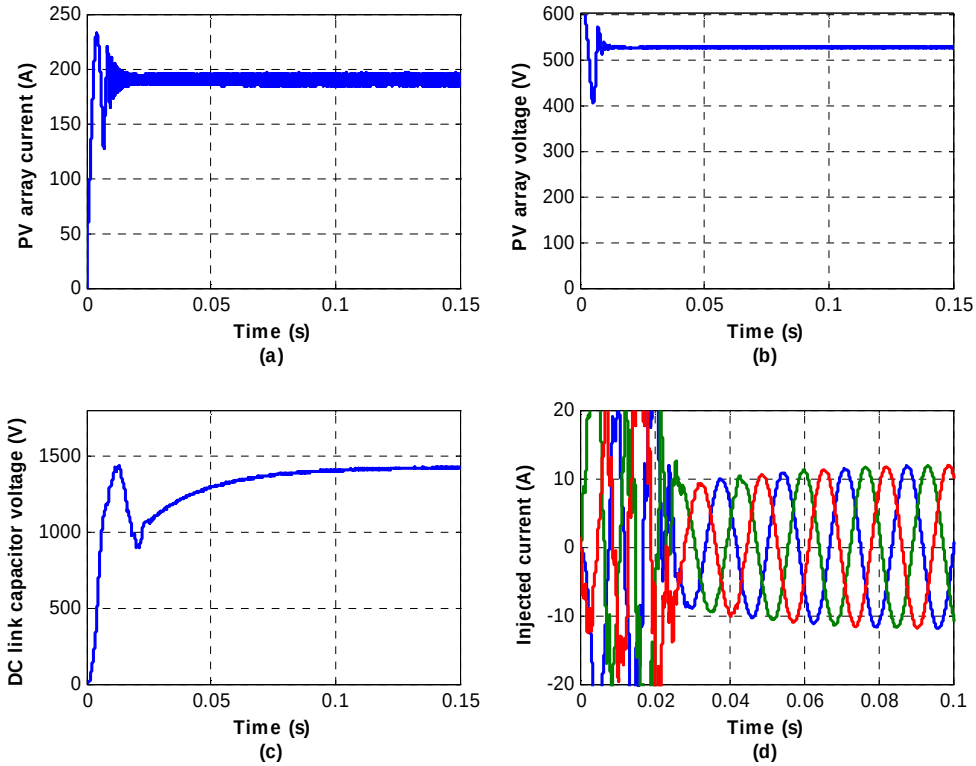

Figure 4-1: (a) DC current output of the PV array (b) Terminal voltage of the array (c) DC link capacitor voltage and (d) injected AC currents at the secondary side of the transformer (grid)

The DC link voltage was monitored to verify the operation of the DC link controller and make sure it reached a constant value for the VSI to operate correctly and generate the required output currents. The purpose of the controller was to force the mismatch between the capacitor input and output DC power to zero. The output of the controller was the reference direct current responsible for setting the output power from the inverter. It took about 0.1 seconds or 6 cycles for the capacitor to reach a steady state voltage of 1400 V as shown in figure 4-1 (c). This fixed voltage DC bus would feed the required power to the inverter to inject the sinusoidal AC currents shown in figure 4-1 (d). These

currents suffered from transients at the start of system operation as the PLL synchronized the control system and due to having a changing DC link capacitor voltage.

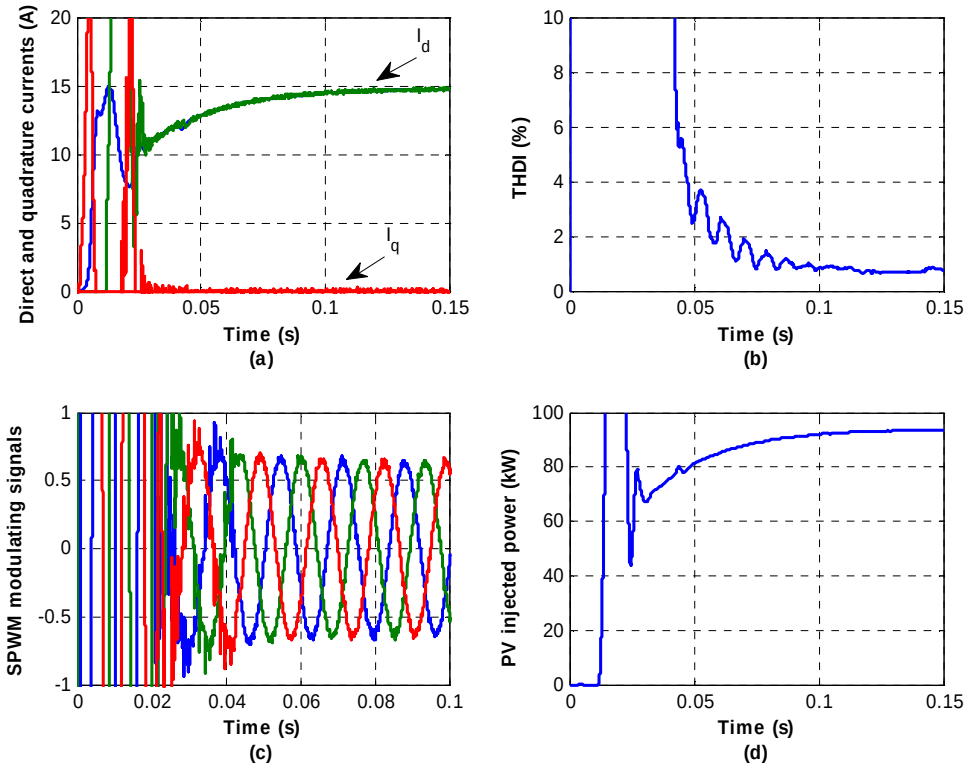

Figure 4-2: (a) dq components of the injected current (b) total harmonic distortion of the output AC current (c) SPWM modulation signals used to drive the VSI and (d) real power delivered to the grid from the PV system

The dq components of the output current are shown in figure 4-2 (a). The quadrature current component responsible for controlling the reactive power output from the inverter was forced to zero in order to achieve unity power factor operation. The direct component was controlled to follow the reference signal set by the DC link voltage controller. The THD level in the output current was below

the limits specified by the IEEE standard 929-2000 which is 5%. The filter connected to the inverter was a low pass type set to attenuate harmonics above 612 Hz in the output. The value of THDI was 1% during steady state operating conditions as shown in figure 4-2 (b). The sinusoidal pulse width modulation signals obtained from the inverter current controller were used to provide the triggering pulses for the inverter switches. The amplitudes of the signals were below unity to ensure over modulation did not occur causing undesirable harmonics in the output. The signals are shown in figure 4-2 (c). The output real power in kW injected into the grid is shown in figure 4-2 (d). The maximum output power form the array under the stated conditions (1000 W/m2 and 25 C) should have been 100 kW. However, due to the estimation of the maximum power point and power losses in harmonics at the inverter output, the actual injected power to the system was 94 kW. From initial results, the open loop MPPT algorithm based on the fractional open circuit voltage technique proved its quick response at system start up in a short time of about 6 cycles as compared to the modified incremental conductance algorithm used in [14].

The switching signal of the boost converter was monitored to examine its duty cycle and switching frequency. In figure 4-3 (a), the duty cycle of the switching signal is about 0.5 during the initial transient phase of the simulation. The switching frequency is around 150 Hz at that point but it increases as the converter drove the PV array close to the maximum power point voltage. During the steady state operation phase which is achieved after the MPP has been located, the switching frequency settles at about 3 kHz. This is shown in figure 4-3 (b) where the duty cycle of the switching signal is at 0.67. In this case, the duty cycle is controlled indirectly by monitoring the PV array terminal voltage and the estimated MPP voltage. Direct control of the duty cycle can be achieved by augmenting this MPPT tracking technique with the IncCond technique in order to fine tune the obtained MPP estimated voltage.

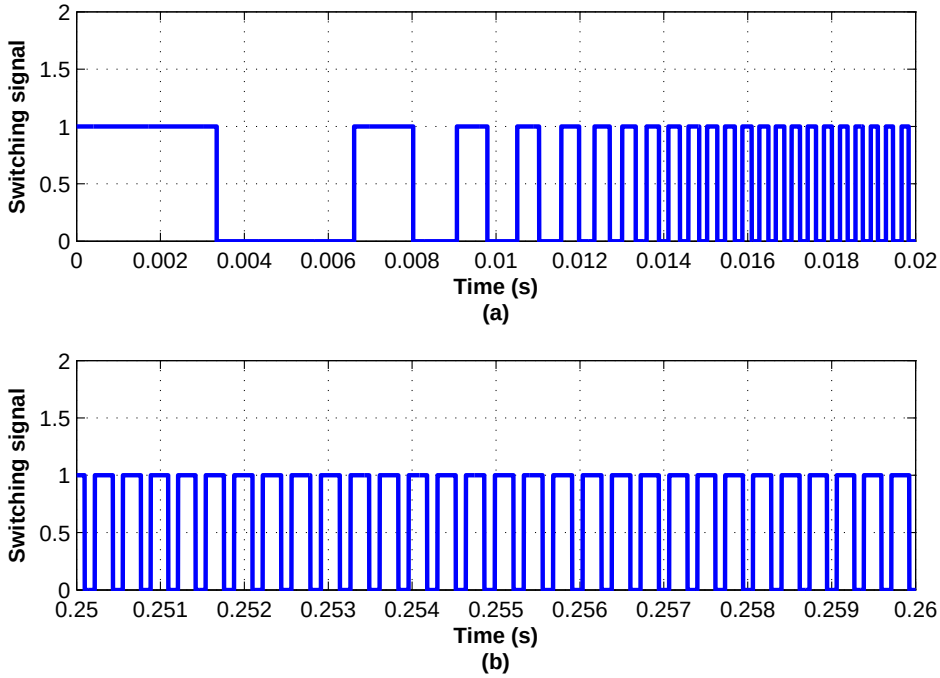

Figure 4-3: (a) switching signal of the boost converter during the tracking phase of the MPP (b) switching signal during steady state after locating the maximum power point of the PV array

4.2 Simulation when *G* changes from 1000 to 500 W/m^2

The goal of the simulation study in this section was to verify the dynamic and steady state response of the control system of the PV array as solar irradiation level dropped rapidly. This is a situation that can happen when a cloud passes by and blocks direct sunlight from hitting the PV array. The array was subjected to a sudden drop in solar irradiation from 1000 to 500 W/m^2 while monitoring the DC and AC voltages and currents in the PV array and the associated power conditioning system. Irradiation level dropped at 0.15 seconds and had an immediate effect on the array DC output current and voltage as shown in figure 4-4 (a) and (b) respectively. The estimated voltage changed due to shading of the array causing the DC converter to move the operating voltage to a new value that corresponded to the new maximum power point, around 500 volts. Array current, which is heavily

dependent on solar irradiation level, dropped to half its initial value at 1000 W/m^2 to about 94 A. This caused the maximum theoretical output power to be halved as well to 50 kW.

As the input power to the DC link capacitor decreased, the DC link controller worked on setting a new reference current for the inverter to match the output power to a new control set point. The capacitor voltage decreased as shown in figure 4-4 (c). It took the controller about 6 cycles to stabilize the capacitor voltage. The injected AC currents experienced a change in amplitude as the reference current was set to a lower value due to the drop in input power, as shown in figure 4-4 (d)

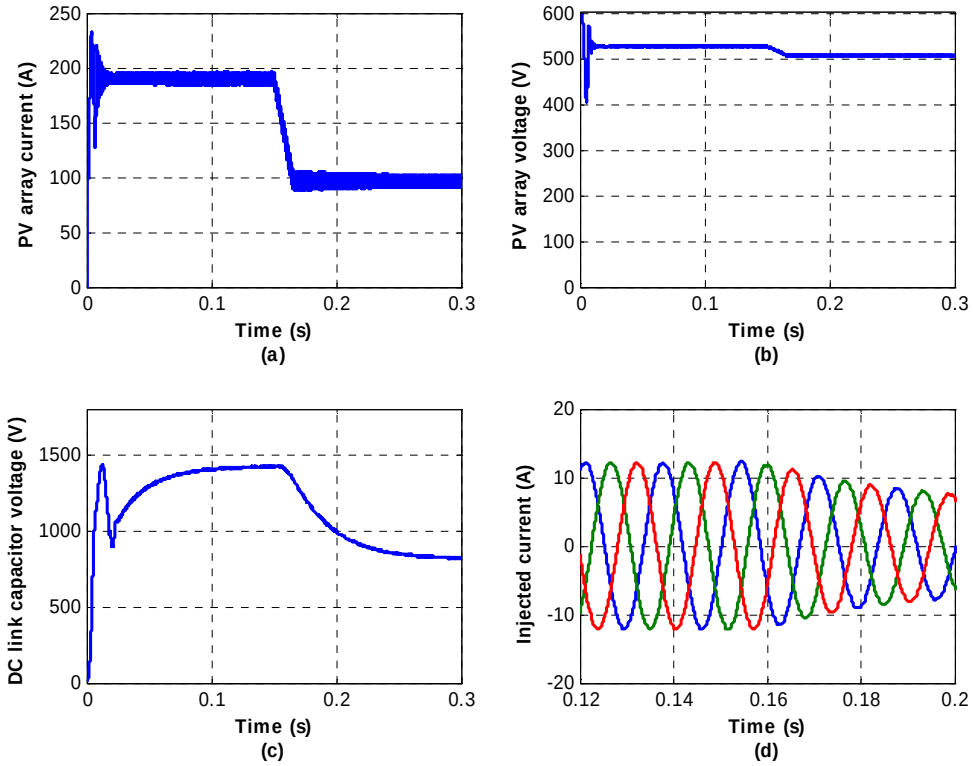

Figure 4-4: (a) DC output current from the array taking into account the change in solar irradiation (b) PV array terminal voltage (c) DC link capacitor voltage and (d) injected AC currents to the grid.

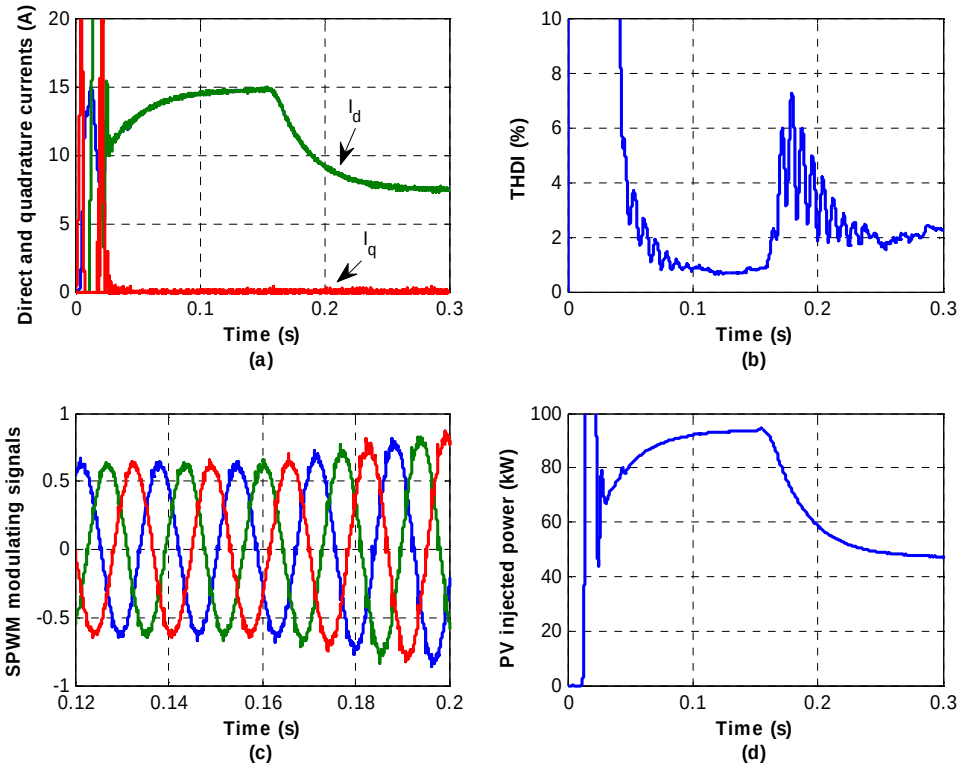

Figure 4-5: (a) dq components of the injected current after the drop in solar irradiation (b) total harmonic distortion in the injected current (c) SPWM modulating signals that drive the inverter switches and (d) real power injected into the grid.

The direct component of the injected current was controlled to follow the new reference value dictated by the DC link controller at 7 A, which dropped from 15 A when solar irradiation was at 1000 W/m^2. The reference for the quadrature component, however, stayed at zero to maintain unity PF operation. The dq components of the injected current are shown in 4-5 (a). The total harmonic distortion in the output current increased during the transition caused by changes in irradiation level as shown in figure 4-5 (b). The current waveform was distorted as it changed to a lower magnitude because of PV power drop. After the transition was complete, the THD reached a level of 2%, an

increase of 1% from the case when solar irradiation was at 1000 W/m^2. The increase in THDI was attributed to the decrease in the magnitude of the injected current where the effect of harmonics was more pronounced.

As the magnitude of the DC link voltage decreased, the sinusoidal PWM signals magnitudes increased to control the inverter to inject the required maximum power to the grid. The signals are shown in figure 4-5 (c). The real output power of the system was recorded to verify the operation of the MPPT technique. Before the drop in solar irradiation, output power from the array was 94 kW from a theoretical maximum of 100 kW. After irradiation dropped, output power was at 47 kW from a theoretical maximum of 50 kW as in figure 4-5 (d). The control system kept track of the approximate maximum power point and responded quickly to the irradiation level change in 0.1 seconds.

4.3 Simulation of the system under fault conditions

The aim of this section is to study the behavior of the grid connected PV system during fault conditions. As stated earlier, the fault current contribution of the grid can be affected by the connection of the PV system. Protection equipment may not respond correctly to faults that occur after the interconnection point of the PV system. A single line to ground fault was simulated at location F shown in figure 3-1. This represented an unbalanced fault type were fault currents have a path through ground. A grounding connection in the PV interfacing transformer can cause this current to circulate back to the system and alter the grid fault current contribution.

4.3.1 Three phase fault: base case

The system was simulated with a three phase fault to determine the fault current level at location F. The fault started at 0.12 seconds and was about 1450 A as shown in figure 4-6 (a). This value was used to set the protection equipment, phase overcurrent relays, to control the substation circuit breaker and isolate the fault. It took 0.1 seconds for the circuit breaker to receive the relay signal and

operate at the next zero crossing in the fault current. The circuit breaker switching position is shown in figure 4-6 (b) where a '1' corresponds to the switch in the closed position and a '0' for being opened.

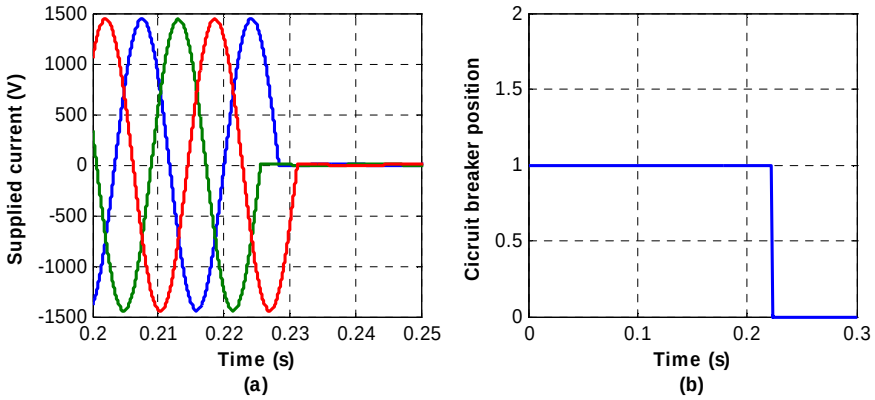

Figure 4-6: (a) Three phase fault at location F in fig 3-1 (b) circuit breaker switching position

4.3.2 SLG fault during PV system connection (Delta –Delta)

The PV system was connected to the grid through a Delta-Delta transformer and the simulation was conducted again to check for the effect it may have on the operation of the protection equipment. The simulation started by setting the fault start time to 0.12 seconds, it was a single line to ground fault in phase A at location F which was set to end at 0.3 seconds. The delta-delta transformer of the PV system did not provide a path for any returning fault current to flow back to the system at the point of common coupling. The circuit breaker operation was therefore unaffected as shown in figure 4-7 (a) where it interrupted the fault at 0.22 seconds. After the circuit breaker opened, the current supplied by the grid to the fault was interrupted at the next zero crossing as shown in 4-7 (b). The fault was successfully terminated at 0.23 seconds as in 4-7 (c). For the duration the fault existed in the system, the PV injected current suffered from high distortion due to the voltage unbalance at the PCC. The phase locked loop output signals were distorted as a result, causing the current control loops to output

highly distorted currents. The injected current waveform is shown in figure 4-7 (d) before and after the fault.

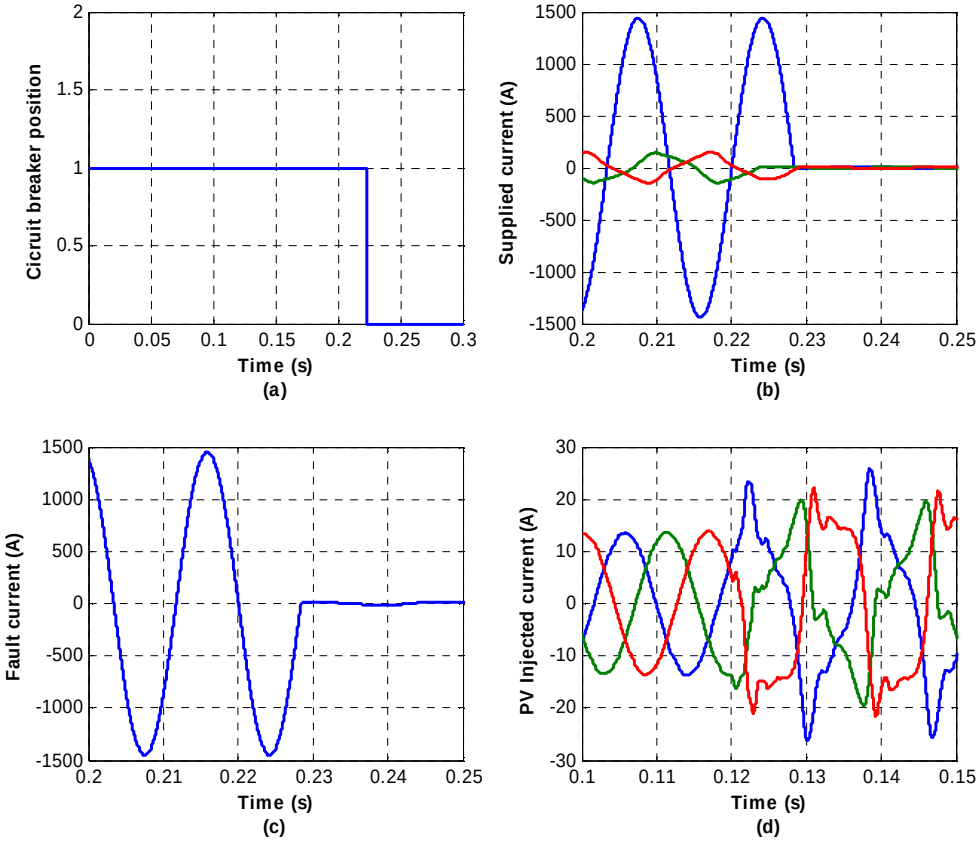

Figure 4-7: (a) circuit breaker switch position '1' for closed and '0' for opened (b) grid supplied current before and after the fault was cleared (c) phase A fault current (d) PV system injected current before and after the fault in phase A.

4.3.3 SLG fault during PV system connection (Delta –Wye gnd)

Replacing the delta-delta with a delta-wye gnd (grid side) transformer caused a problem for the phase overcurrent relays detecting the fault. The fault started at the same time, 0.12 seconds, and was also set to end at 0.3 seconds. The circuit breaker failed to isolate the fault and remained closed for the

entire fault duration as shown in figure 4-8 (a). The grounding connection of the transformer at the grid side caused fault current to return back to the grid at the point of common coupling. This zero sequence current was divided equally between the three phases at the secondary side of the transformer and injected back to the grid. These currents interacted with the grid supplied current and caused it to drop below the set point for the overcurrent relays as shown in figure 4-8 (b). The fault current continued without interruption as shown in figure 4-8 (c) while the current output of the PV system transformer is shown in figure 4-8 (d).

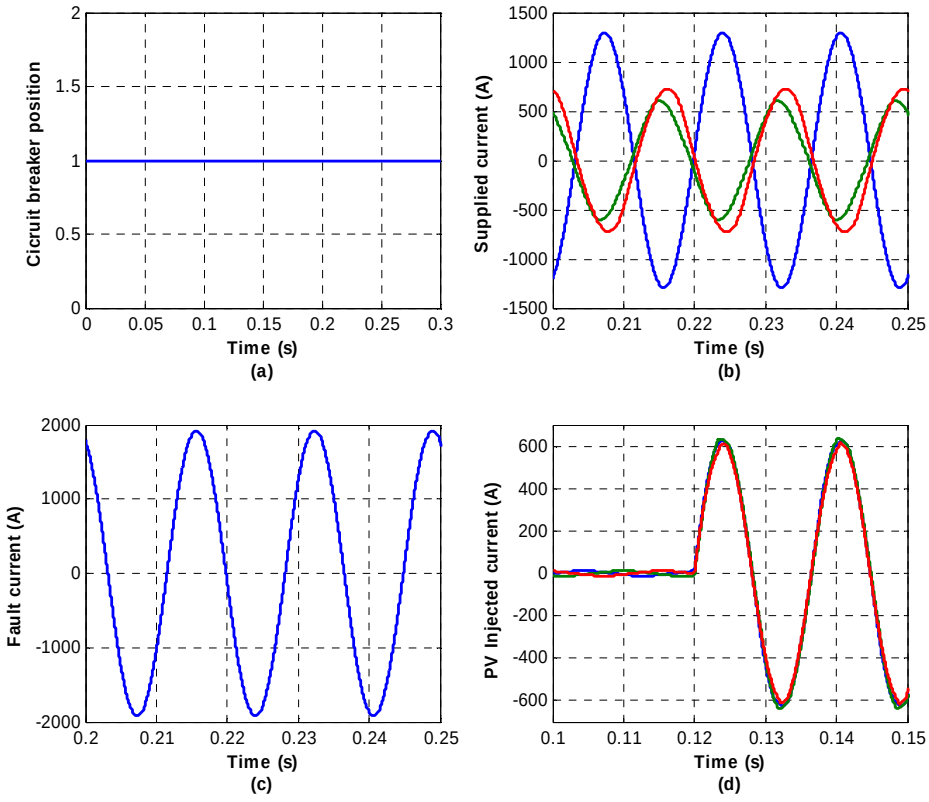

Figure 4-8: (a) circuit breaker switch position '1' for closed and '0' for opened (b) grid supplied current during the SLG fault (c) phase A fault current (d) output current from the PV system transformer

4.3.4 Simulation under a three phase symmetrical fault

The system was studied under a three phase symmetrical fault. During a three phase symmetric fault condition, no zero sequence currents existed and the interfacing transformer did not cause any currents to circulate back to the grid. The circuit breaker isolated the fault at 0.22 seconds as shown in figure 4-9 (a) after receiving a control signal from the overcurrent relay. The current supplied by the grid during fault conditions shown in figure 4-9 (b) was not affected by the connection of the PV system. The injected current by the PV system, shown in figure 4-9 (d), increased during the fault due to the drop in the grid voltage. The increase was not significant to disrupt the operation of the relay.

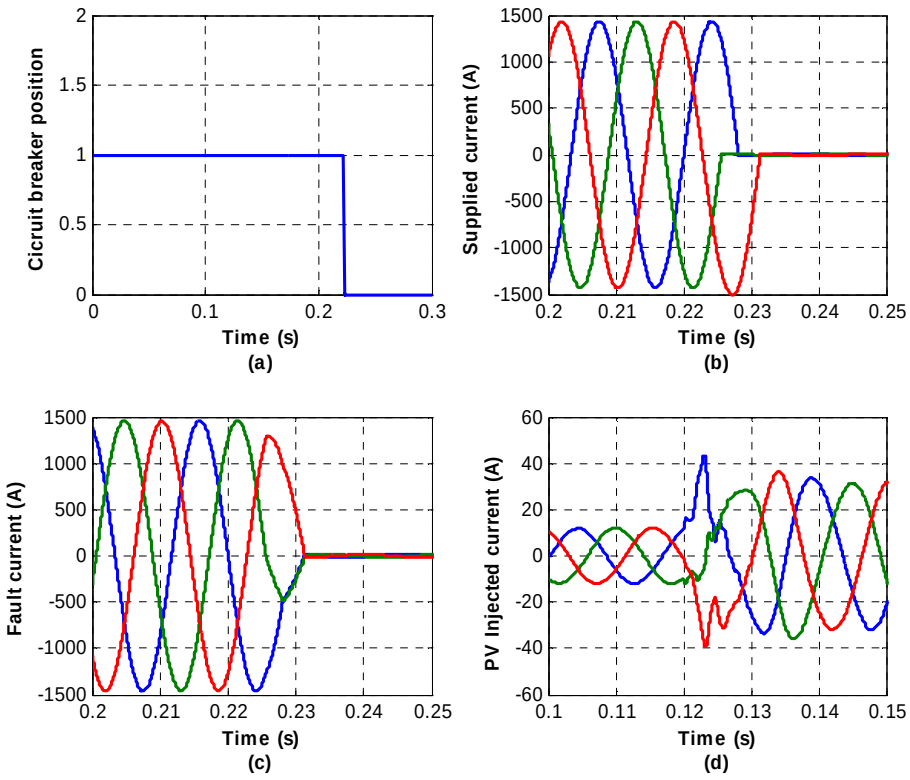

Figure 4-9: (a) circuit breaker switch position '1' for closed and '0' for opened (b) grid supplied current during the three phase fault (c) 3 phase fault current (d) output current from the PV system transformer

Chapter 5
Conclusion and future work

5.1 Conclusion

The design of a control system for three phase grid connected photovoltaic arrays was detailed in this thesis. The open loop maximum power point tracking technique aimed at solving the problems present in two of the most common techniques used for that purpose: the perturb and observe (P&O) and incremental conductance algorithms. The main drawbacks of the P&O technique are its poor dynamic response and swinging around the maximum power point during steady state operation. During fast changes in atmospheric conditions, the P&O technique may erroneously move in the wrong direction on the PV power curve if each perturbation caused power to increase. The other issue is the steady state swing it has when it reaches the maximum power point as it perturbs the duty cycle of a DC converter to check for power variations.

The incremental conductance technique suffers also from a relatively slow dynamic response time. In each control step it is required to carry some computations to calculate the instantaneous and incremental conductance and then compare them to each other. Although it has an improved response time than the P&O technique, it is difficult to implement that technique in grid connected systems in its basic form.

The open loop MPPT technique employed in this thesis aims at providing an improved dynamic response time as compared to the previously mentioned techniques. It does not suffer from high implementation complexity as well. The PV array maximum power point was approximated using test PV cells that kept track of the current weather conditions.

A DC link voltage controller was presented in order to solve the problem of regulating the voltage at the input of the three phase VSI. This problem arises due to the nonlinear characteristics of the PV

array. By matching input and output powers of the DC link capacitor, its voltage can be fixed at a constant value for the inverter to operate correctly and produce AC output voltages that can be controlled in magnitude.

Finally, a fault study was conducted to assess the impact of the grid connected PV system on the protection devices of the power system it is connected to. This is important as the number of distributed generation sources connected to the system increase and contribute a significant amount of power that it becomes difficult to isolate them during a fault. The topology of the interfacing transformer of the PV system played a significant role in providing a path for returning fault current back to the grid. In order to compensate for the effect of DG fault current injections, the pick-up current of the protective relays needs to be decreased in order to accommodate the reduced fault current contribution from the utility.

5.2 Future work

The operation of photovoltaic arrays encompasses several issues that need to be considered to further improve the operation of the control system. Future work can be carried on to expand the scope of this research; this can be summarized into the following points:

1. Incorporation of the partial shading effect of PV arrays. This problem arises when sunlight is blocked from hitting a section of a PV array directly while other sections continue their normal operation. The estimation process of the PV array open circuit voltage will not be accurate and this will cause significant deviations from the maximum power point. The control system should be able to detect this situation and carry out any required corrections to improve the estimation process. This control requirement should be carried on close to real time in order to avoid any delays that would degrade the dynamic response of the algorithm.

2. Improve the operation of the open loop MPPT algorithm by combining it with the incremental conductance technique. The major benefit of using the open loop technique is the speed it acquires the MPP estimation. During steady state, it might not operate exactly at the maximum power point. By adding the IncCond algorithm into the control scheme, steady state response can be improved and operation at the exact maximum power point can be achieved.

3. Power sharing control between a mix of distributed generation sources that include PV arrays. A control strategy is required to organize the operation of dispatchable and non-dispatchable (i.e.: renewable energy sources) sources to reduce operating and fuel costs. The output power from dispatchable DG sources can be controlled, which is not possible for renewable energy sources that depend on weather conditions like wind or sunlight. When there is an abundance of sunlight, PV arrays output power can be maximized while reducing power output from the controllable DG sources to save fuel.

References

[1] US Energy Information Adminstration (EIA). (2010). International Energy outlook [Online]. Available: http://www.eia.doe.gov/oiaf/ieo/highlights.html

[2] International Energy Agency (IEA)-PVPS. (2009, Sept.). Trends in photovoltaic applications. [Online]. Available: www.iea-pvps.org

[3] Ontario Power Authority (2010, August). Renewable energy feed-in tariff Program. [Online]. Available: fit.powerauthority.on.ca

[4] Masters, Gilbert M., Renewable and efficient electric power systems. John Wiley & Sons, 2004

[5] US Department of Energy (DOE). (2010). Solar Energy Technologies Program. [Online]. Available: http://www1.eere.energy.gov/solar/pv_devices.html

[6] J.A. Gow, C. Manning, "Development of a photovoltaic array model for use in power-electronics simulation studies," in proc. IEE Electric power applications, vol 146, issue 2, pp.193-200, March 1999.

[7] M. G. Villalva, et al., "Comprehensive Approach to Modeling and Simulation of Photovoltaic Arrays," IEEE Transactions on Power Electronics, vol. 24, pp. 1198-1208, 2009.

[8] S. B. Kjaer, J. K. Pedersen, and F. Blaabjerg, “A review of single-phase grid-connected inverters for photovoltaic modules,” IEEE Trans. Ind. Appl., vol. 41, no. 5, pp. 1292–1306, Sep./Oct. 2005.

[9] I. Atlas, A. Sharaf "A photovoltaic array simulation model for Matlab Simulink GUI environment," in international Conf. on Clean Electrical Power, pp.341-345, May 2007.

[10] Shengyi Liu; Dougal, R.A.; , "Dynamic multiphysics model for solar array," *IEEE Transactions on Energy Conversion*, vol.17, no.2, pp.285-294, Jun 2002

[11] Wu, Bin High-Power Converters and AC Drives. John Wiley & Sons, 2006.

[12] T. Esram and P. L. Chapman, "Comparison of Photovoltaic Array Maximum Power Point Tracking Techniques," IEEE Transactions on Energy Conversion, vol. 22, pp. 439-449, 2007.

[13] Femia, N.; Petrone, G.; Spagnuolo, G.; Vitelli, M.;, "Optimization of perturb and observe maximum power point tracking method," IEEE Transactions on Power Electronics, vol.20, no.4, pp. 963- 973, July 2005

[14] Weidong Xiao; Dunford, W.G.;, "A modified adaptive hill climbing MPPT method for photovoltaic power systems," 35th IEEE Annual Power Electronics Specialists Conference. PESC 04. vol.3, no., pp. 1957- 1963 Vol.3, 20-25 June 2004

[15] D'Souza, N.S.; Lopes, L.A.C.; Xuejun Liu; , "An Intelligent Maximum Power Point Tracker Using Peak Current Control," 36th IEEE Power Electronics Specialists Conference, 2005. PESC '05, vol., no., pp.172, 16-16 June 2005

[16] Hussein, K.H.; Muta, I.; Hoshino, T.; Osakada, M.;, "Maximum photovoltaic power tracking: an algorithm for rapidly changing atmospheric conditions," IEE Proceedings on Generation, Transmission and Distribution, vol.142, no.1, pp.59-64, Jan 1995.

[17] Tae-Yeop Kim; Ho-Gyun Ahn; Seung Kyu Park; Youn-Kyun Lee; , "A novel maximum power point tracking control for photovoltaic power system under rapidly changing solar radiation," IEEE International Symposium on Industrial Electronics., vol.2, no., pp.1011-1014 vol.2, 2001

[18] Khaehintung, N.; Pramotung, K.; Tuvirat, B.; Sirisuk, P.;, "RISC-microcontroller built-in fuzzy logic controller of maximum power point tracking for solar-powered light-flasher applications," 30th Annual Conference of IEEE Industrial Electronics Society. IECON 2004., vol.3, no., pp. 2673- 2678 Vol. 3, 2-6 Nov. 2004.

[19] Chung-Yuen Won; Duk-Heon Kim; Sei-Chan Kim; Won-Sam Kim; Hack-Sung Kim; , "A new maximum power point tracker of photovoltaic arrays using fuzzy controller," ., 25th Annual IEEE Power Electronics Specialists Conference, PESC '94, pp.396-403 vol.1, 20-25 Jun 1994

[20] Patcharaprakiti, N.; Premrudeepreechacharn, S.;, "Maximum power point tracking using adaptive fuzzy logic control for grid-connected photovoltaic system," IEEE Power Engineering Society Winter Meeting, vol.1, no., pp. 372- 377 vol.1, 2002

[21] Zhang, L.; Yunfei Bai; Al-Amoudi, A.; , "GA-RBF neural network based maximum power point tracking for grid-connected photovoltaic systems,", International Conference on Power Electronics, Machines and Drives, vol., no., pp. 18- 23, 4-8 June 2002

[22] Hiyama, T.; Kouzuma, S.; Imakubo, T.;, "Identification of optimal operating point of PV modules using neural network for real time maximum power tracking control," IEEE Transactions on Energy Conversion, vol.10, no.2, pp.360-367, Jun 1995

[23] Kroutikova, N.; Hernandez-Aramburo, C.A.; Green, T.C.;, "State-space model of grid-connected inverters under current control mode," Electric Power Applications, IET , vol.1, no.3, pp.329-338, May 2007

[24] Kawabata, T.; Miyashita, T.; Yamamoto, Y.; , "Dead beat control of three phase PWM inverter," IEEE Transactions on Power Electronics, vol.5, no.1, pp.21-28, Jan 1990

[25] Danish Energy Authority (2008). Facts about wind power. [Online]. Available: http://www.ens.dk/en-US/Sider/forside.aspx

[26] "IEEE Recommended Practice for Utility Interface of Photovoltaic (PV) Systems," IEEE Std 929-2000, p. i, 2000.

[27] Selvaraj, J.; Rahim, N.A.; , "Multilevel Inverter For Grid-Connected PV System Employing Digital PI Controller," , IEEE Transactions on Industrial Electronics, vol.56, no.1, pp.149-158, Jan. 2009

[28] Castilla, M.; Miret, J.; Matas, J.; Garcia de Vicuna, L.; Guerrero, J.M.; , "Control Design Guidelines for Single-Phase Grid-Connected Photovoltaic Inverters With Damped Resonant Harmonic Compensators," , IEEE Transactions on Industrial Electronics, vol.56, no.11, pp.4492-4501, Nov. 2009.

[29] Patel, H.; Agarwal, V.; , "MPPT Scheme for a PV-Fed Single-Phase Single-Stage Grid-Connected Inverter Operating in CCM With Only One Current Sensor," IEEE Transactions on Energy Conversion, vol.24, no.1, pp.256-263, March 2009

[30] S. B. Kjaer, J. K. Pedersen, and F. Blaabjerg, "A review of single-phase grid-connected inverters for photovoltaic modules," IEEE Trans. Ind. Appl., vol. 41, no. 5, pp. 1292–1306, Sep./Oct. 2005.

[31] M. P. Kazmierkowski and L. Malesani, "Current control techniques for three-phase voltage-source PWM converters: a survey," IEEE Transactions on Industrial Electronics, vol. 45, pp. 691-703, 1998.

[32] Y. Mohamed and E. F. El-Saadany, "Adaptive Decentralized Droop Controller to Preserve Power Sharing Stability of Paralleled Inverters in Distributed Generation Microgrids," IEEE Transactions on Power Electronics, vol. 23, pp. 2806-2816, 2008.

[33] A. Timbus, et al., "Evaluation of Current Controllers for Distributed Power Generation Systems," IEEE Transactions on Power Electronics, vol. 24, pp. 654-664, 2009.

[34] Zeman, M.;, "New trends in thin-film silicon solar cell technology," The Fourth International Conference on Advanced Semiconductor Devices and Microsystems, vol., no., pp. 353- 362, 14-16 Oct. 2002

[35] Natural Resources Canada (2007). Protection Coordination Planning with Distributed Generation. [Online]. Available: canmetenergy-canmetenergie.nrcan-rncan.gc.ca/fichier.php/codectec/En/2007-149/ 2007-149e.pdf

[36] M. K. Mishra, et al., "Operation of a DSTATCOM in Voltage Control Mode," IEEE Power Engineering Review, vol. 22, pp. 79-79, 2002.

[37] F. Blaabjerg, et al., "Overview of Control and Grid Synchronization for Distributed Power Generation Systems," IEEE Transactions on Industrial Electronics, vol. 53, pp. 1398-1409, 2006.

[38] M. Marei, E. El-Saadany, M. Salama, "Flexible distributed generation: FDG," in IEEE power Engineering Society Summer Meeting, vol 1, pp. 49-53, July 2002.

[39] M. Marei, E. El-Saadany, and M. Salama, “A novel control algorithm for the DG interface to mitigate power quality problems," IEEE Transactions on Power Delivery, vol. 19, pp. 1384-1392, July 2004.

[40] F. Katiraei and M. R. Iravani, “Power management strategies for a microgird with multiple distributed generation units," IEEE Transactions on Power Systems, vol. 21, pp. 1821-1831, Nov. 2006.

Appendix A

System data

Grid voltage, line to line (rms)	6.6 kV
Photvoltaic array	
maximum output power	100 kW
series modules	20
parallel strings	25
MPP voltage	526 V
DC link capacitor controller	
Kp	1
Ki	460
C	2000 uF
Phase locked loop	
Kp	2.1
Ki	5000
Current controllers	
Kp	30
Ki	20000
Interfacing transformer	
Primary voltage (PV side)	500 V
Secondary voltage (grid side)	6.6 kV
RL Load	
appearent power (S)	1.11 MVA
power factor	0.9
Filter	
L	1.35 mH
C	50 uF